Article

High Spatiotemporal-Resolution Magnetic Tweezers: Calibration and Applications for DNA Dynamics

David Dulin,[1,*] Tao Ju Cui,[1] Jelmer Cnossen,[1] Margreet W. Docter,[1] Jan Lipfert,[2] and Nynke H. Dekker[1,*]
[1]Department of Bionanoscience, Kavli Institute of Nanoscience, Delft University of Technology, Delft, The Netherlands; and [2]Department of Physics, Nanosystems Initiative Munich and Center for Nanoscience, Ludwig-Maximilians-University Munich, Munich, Germany

ABSTRACT The observation of biological processes at the molecular scale in real time requires high spatial and temporal resolution. Magnetic tweezers are straightforward to implement, free of radiation or photodamage, and provide ample multiplexing capability, but their spatiotemporal resolution has lagged behind that of other single-molecule manipulation techniques, notably optical tweezers and AFM. Here, we present, to our knowledge, a new high-resolution magnetic tweezers apparatus. We systematically characterize the achievable spatiotemporal resolution for both incoherent and coherent light sources, different types and sizes of beads, and different types and lengths of tethered molecules. Using a bright coherent laser source for illumination and tracking at 6 kHz, we resolve 3 Å steps with a 1 s period for surface-melted beads and 5 Å steps with a 0.5 s period for double-stranded-dsDNA-tethered beads, in good agreement with a model of stochastic bead motion in the magnetic tweezers. We demonstrate how this instrument can be used to monitor the opening and closing of a DNA hairpin on millisecond timescales in real time, together with attendant changes in the hairpin dynamics upon the addition of deoxythymidine triphosphate. Our approach opens up the possibility of observing biological events at submillisecond timescales with subnanometer resolution using camera-based detection.

INTRODUCTION

In the cell, numerous enzymes are involved in molecular transport or nucleic acid metabolism (1). At the level of individual molecules, the activities of these enzymes are intrinsically stochastic and highly dynamic (2), and the goal of characterizing their activities in detail has spurred the development of novel biophysical approaches (3). The continuous improvement of such approaches over the past two decades has made it possible to resolve ever-smaller steps of enzymatic motion on ever-shorter timescales (4–7). These advances have furthered our understanding of enzymatic processes by revealing how forces, torques, mechanochemistry, and intrinsic stochasticity conspire to impact the behavior of individual molecules (3,8–12); they have also shed light on the processes of replication, transcription, and translation that underlie the central dogma. Such studies have revealed, for example, the coordination between the proteins involved in phage or bacterial replisomes (13), the mechanism of initiation in bacterial RNA polymerase (14,15), the intrinsic dynamics of RNA polymerase elongation (16), and the genome packaging dynamics by phage proteins (17). Enzymes that employ DNA or RNA as their template or substrate typically have a characteristic step size close to the size of a DNA basepair (bp), i.e., 0.34 nm for double-stranded DNA (dsDNA) in its B-form. Often these enzymes advance at rates of 20 bp/s or faster in vivo (with similar rates observed in in vitro measurements (16,18)), implying that a DNA basepair is processed within ~50 ms. To fully resolve the details of such enzymatic motion (including, e.g., an enzyme's step size) under physiological conditions, it is therefore necessary to detect motion on these timescales with a spatial resolution of ~0.3 nm or better.

A variety of high-resolution single-molecule techniques, including single-molecule fluorescence resonance energy transfer (FRET) (5,19), optical tweezers (20–22), and magnetic tweezers (MT) (23,24) have been developed to observe individual enzymatic steps (3). Although the donor-acceptor fluorophore interaction that underlies FRET provides a sensitive molecular ruler with which to observe macromolecular conformational changes, this technique does not permit the mechanical manipulation of molecules as do optical tweezers and MT. Optical tweezers implemented in a dumbbell configuration have achieved the best spatiotemporal resolution to date in an enzymatic study. In this assay, the positions of two trapped microspheres linked together by a nucleic acid are controlled, allowing enzymatic activity on the nucleic acid to be read out from the displacement of the beads from their equilibrium positions (7). Block and coworkers have harnessed such an apparatus to resolve the stepping behavior of *Escherichia coli* RNA polymerase at 1 bp/s (20,21), and Bustamante and co-workers utilized it

Submitted February 18, 2015, and accepted for publication October 13, 2015.

*Correspondence: daviddulin82@gmail.com or n.h.dekker@tudelft.nl

David Dulin's present address is Biological Physics Research Group, Clarendon Laboratory, Department of Physics, University of Oxford, Oxford, United Kingdom.

Editor: Keir Neuman.

0006-3495/15/11/2113/13

http://dx.doi.org/10.1016/j.bpj.2015.10.018

to observe the translocation of the ϕ29 DNA packaging motor (25) (and later, using a simplified apparatus, the NS3-hepatitis C RNA helicase (22)). Although these experiments achieved high spatiotemporal resolution, their resolution does not yet suffice to observe basepair stepping under physiological conditions (4). In addition, the observation of rare events such as nucleotide misincorporation necessitates very large data sets, which are difficult to obtain using optical tweezers, as they are cumbersome to multiplex.

In MT experiments, the molecule of interest is tethered between a surface and a superparamagnetic bead, and force is applied via an external magnetic field (Fig. 1). Standard magnetic tweezers track the position of beads at an acquisition frequency of ~50–100 Hz and can resolve the position of a surface-melted bead along the z axis to ~1 nm (26,27). However, recent improvements to MT based on high-speed complementary metal-oxide semiconductor (CMOS) cameras have enhanced the resolution to the sub-Ångstrom level at 1 s bandwidth on individual beads (28,29). In addition, magnetic tweezers, with their use of camera-based detection and ability to apply a homogenous force over an entire field of view, facilitate the simultaneous tracking of hundreds of molecules (26,30,31). Improving the spatiotemporal resolution of MT therefore presents an important step toward multiplexed measurements at high resolution.

In this work, we introduce an MT configuration that combines high spatial and temporal resolution (26,28,29) while maintaining all the existing advantages of this technique: straightforward implementation necessitating only a limited number of optical elements, a relatively drift-insensitive apparatus, spatial information via camera-based detection, and natural operation as a stable force clamp. We have combined several recent technical advances to make this development possible. First, recent improvements in CMOS cameras enable fast image acquisition (at better than kHz) which, when combined with a high intensity illumination source, allows one to average over the dominant source of noise in camera-based detection, namely, the tracking noise (28,29). Although such camera-based tracking is in principle straightforward, its use in tracking microspheres involves the use of many pixels, which reduces the achievable tracking speed. Parallelization of the computational process that underlies real-time tracking of microsphere position is therefore highly desirable. Such parallelization is greatly facilitated by a second advance, namely, the use of graphics processor unit (GPU) computation. The use of GPUs makes it possible to perform three-dimensional bead-position tracking in real time at approximately kHz rates, as we and others have demonstrated (26,29). A remaining challenge has been to achieve sufficient illumination intensity to utilize the camera's entire dynamic range on submillisecond timescales. Applying recent developments in laser-based illumination sources (32), we demonstrate here that the use of a modulated laser provides a highly efficient way to fulfill this criterion. In combining

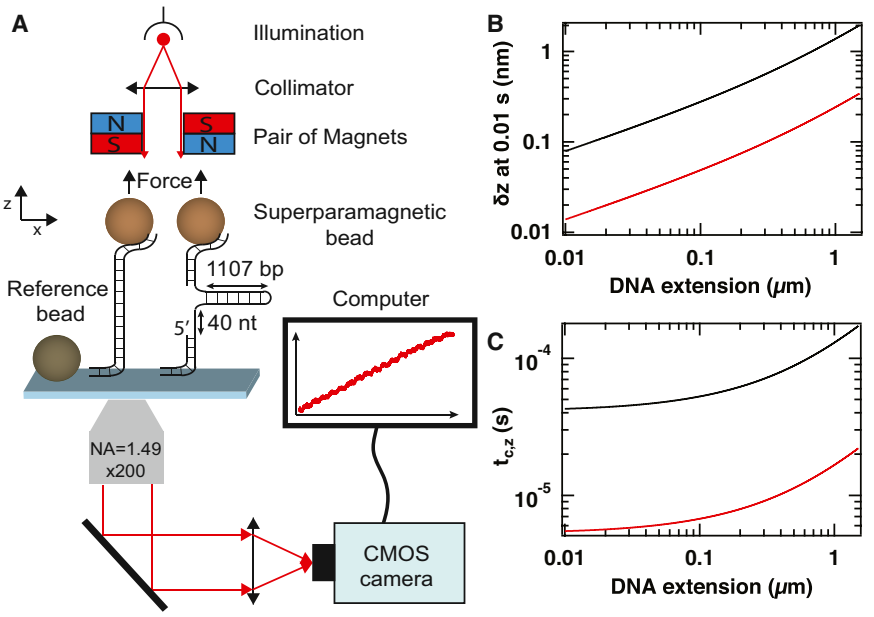

FIGURE 1 Description of the experimental apparatus and computation of the expected spatiotemporal resolution. (*A*) Schematic representation of the experimental setup (not to scale). A pair of magnets in a vertical orientation separated by a gap of either 1 mm or 0.3 mm is placed above a flow cell. The illumination source is either a high-power fiber-coupled LED or a laser diode, and the emitted light is collimated before passing through the gap separating the magnets and illuminating the sample. The tracked beads are superparamagnetic beads tethered to either a 1.9 kb dsDNA or a 1.1 kb hairpin, and latex nonmagnetic reference beads are directly adhered to its surface via melting (Materials and Methods). The hairpin contains a 40 nucleotides ssDNA sequence on one side, as indicated. The dsDNA and hairpin molecules are both attached via ligated DNA handles, one of which includes multiple biotin labels for attachment to the streptavidin-coated magnetic bead and a second that contains multiple digoxigenin labels for attachment to the flow-cell surface. The light is collected by a high-NA objective, and images are projected onto a high-speed CMOS camera via a 400 mm tube lens (see Materials and Methods). The collected frames are transferred first to a frame grabber and then to a computer. They are analyzed using an nVIDIA graphics card at a rate of up to 8 kHz for a single bead. (*B*) Calculation of the standard deviation, δz, at 0.01 s of the z-position of a tethered bead (radius $R = 500$ nm) as a function of the DNA extension at 18 pN applied force, F, for either ssDNA (persistence length $L_p = 0.5$ nm, *black line*) or dsDNA (persistence length $L_p = 50$ nm, *red line*). The equivalent bandwidth, B_{eq}, is set to 100 Hz (Eq. 3). (*C*) Calculation of the characteristic time, $t_{c,z}$, of the bead-tether system at 18 pN according to Eq. 5. All parameters are identical to those in (*B*). To see this figure in color, go online.

these three advances, we develop a high-spatiotemporal-resolution MT configuration that achieves real-time tracking of a single bead in a region of interest of 100 × 100 pixels at 8 kHz for up to 10 min. This allows us to achieve an Allan deviation (AD) in the z-position of ~0.07 nm at 0.01 s for a surface-melted bead, and ~0.2 nm at 1 s for a dsDNA molecule held under a force of 18 pN. We further demonstrate the capabilities of our instrument by observing the opening and closing transitions of a DNA hairpin on millisecond timescales and by showing that the open state of this hairpin is stabilized in the presence of deoxythymidine triphosphate (dTTP). This high-speed, high-resolution MT using laser-based illumination should find numerous applications in the field of nucleic-acids-based motors and other areas of biology.

MATERIALS AND METHODS

Magnetic tweezers instrument

The MT assay is implemented on a custom-designed microscope (Fig. 1 *A*). A pair of vertically aligned permanent magnets (33) separated by a 0.3 mm gap are positioned above the flow cell. The rotation of the magnets and their vertical position are controlled by stepping motors (C-150 and M-126.PD2, respectively, both from Physik Instrumente, Waldbronn, Germany) (34,35). A piezo-controlled nanopositioning stage (P-726, E-712 controller, Physik Instrumente) controls the height of the objective (100×, oil-immersion objective, NA 1.49, Nikon, Tokyo, Japan). The image of the sample plane is imaged via a 400 mm tube lens (achromatic doublet, Newport, RI) onto an 8-bit CMOS camera (MC1362, Mikrotron, Unterschleissheim, Germany), yielding a pixel size in the image plane of ~70 nm. The entire apparatus is placed inside an opaque box that provides shielding against light pollution, acoustic noise, and air currents, and mounted onto an optical table (TMC784, Technical Manufacturing, Peabody, MA). The MT apparatus is controlled using a Dell Precision T3610 computer (Round Rock, TX) operating at 64 bits that includes an Intel Xeon CPU ES-1620 v2 (Santa Clara, CA) with a processor base frequency of 3.70 GHz, 8 GB of RAM memory, and an NVIDIA GeForce GTX 580 graphic card.

Sample illumination

We utilize two configurations for sample illumination. The first illumination configuration employs a high-power fiber-coupled light-emitting diode (LED) (660 nm, M660F1, Thorlabs, Munich, Germany). The fiber output is coupled to a collimator (CFC-5X-B, Thorlabs) that is situated just above the pair of magnets to maximize intensity in the sample plane. The second illumination configuration employs a laser diode (660 nm, 120 mW; HL6545MG, Thorlabs) that is mounted onto an integrated temperature controller (LDM9T, Thorlabs). To this temperature controller, we apply a 2 MHz sinusoidal current modulation via a 50 Ω bias tee and a voltage generator to broaden the laser's emission spectrum. This reduces its temporal coherence and hence the amount of speckle (32). The laser is collimated using an aspheric lens and is then directed toward the sample.

Camera acquisition parameters

The CMOS camera allows the selection of up to four independent regions of interest that can be separately positioned within the field of view. As the maximum frame rate is closely related to the total size of the regions of interest, having independent regions of interest on the camera chip allows for a large increase in the achievable acquisition speed: from 506 Hz for a single full field of view of 1280 × 1024 pixels, to 4 kHz for two independent regions of interest of 100 × 100 pixels. In the latter case, the achievable acquisition frequency becomes limited by the computer processing speed during the transfer of the images from the frame grabber to the graphics card. The camera shutter time is set to the inverse of the acquisition frequency for all measurements. The custom-written software implemented in CUDA and Labview (Labview 2011 SP1, National Instruments, Austin, TX) (26) that has been developed to process camera images for highly multiplexed MT experiments at low frame rate, e.g., 50 Hz maximum, has been adapted for the continuous extraction of tracked bead positions in (x, y, z) in real time over 10 min at an acquisition frequency of 8 kHz (ultimately limited only by the size of the file that stores the three-dimensional positions with their time stamp). However, we typically limit the duration of acquisition to 200 s for ease of manipulation of the resulting data sets.

When we employ laser-based illumination (Fig. S2 *A* in the Supporting Material), we adapt the camera image to correct for any speckle that remains after the fast modulation of the laser and contributes to the graininess of the image (Fig. S2 *B*) (32). This additional source of noise is not suppressible via reference-bead-position subtraction, so instead we implement a per-pixel linear correction where corrected pixel values are computed as pixel' $= a$*(pixel $+ b$). A set of coefficients, a and b, is computed before a measurement for each pixel by selecting a bead-free image and averaging a series of frames at that position. During tracking, the image pixel values are first corrected and the corrected image is then transferred to the tracking algorithm to extract bead positions. This procedure substantially reduces the background noise (Fig. S2 *C*).

Magnetic tweezers flow cell

We employ two types of superparamagnetic beads: 1 μm diameter MyOne beads and 2.8 μm diameter M270 beads (both from Life Technologies, Bleiswijk, The Netherlands). These bead types are selected for their excellent homogeneity in size and magnetic content (30). The applied force is proportional to the magnetic content of the bead (33); therefore, a larger diameter bead typically allows for a higher force. However, under the same applied force, a tether attached to a larger bead has an increased correlation time compared to a similar tether attached to a smaller bead (see Characteristic timescale of z-fluctuations in MT). To permit the application of sufficient force to open a DNA hairpin (~16 pN) while maintaining the advantages of the smaller MyOne beads, we therefore reduce the gap between the magnets to 0.3 mm. Additionally, we minimize the distance between the magnets and the beads by sealing the flow cell (which consists of two thin coverslips—numbered 0 for the top coverslip and 1 for the bottom coverslip; Menzel Glazer, Braunschweig, Germany) using a stretched Parafilm layer (Dupont, Wilmington, DE). The inner bottom surface of the flow cell is coated with a nitrocellulose solution (0.1% m/V in ethanol) that contains a 1:250 dilution of the desired type of reference beads (26). Once coated, the coverslip is baked at 150°C for 3 min, whereupon the flow cell is assembled and sealed as described above.

Construction of the handles for the dsDNA construct

To create biotin- and digoxigenin-labeled handles, a 1.2-kb fragment of pBluescript plasmid (Stratagene/Agilent Technologies, Santa Clara, CA) is amplified by polymerase chain reaction (PCR) using forward primer 5′-GACCGAGATAGGGTTGAGTG and reverse primer 5′-CAGGGTCG GAACAGGAGAGC in the presence of biotin-16-deoxyuridine triphosphate (dUTP) and digoxigenin-11-dUTP (both from Roche Diagnostics, Basel, Switzerland), respectively. The digoxigenin and biotin handles are then digested with *Eco*RI and *Xho*I, respectively.

Assembly of a fully tetherable 1.9 kb dsDNA construct

To form the core of the dsDNA construct, a 1.9 kb fragment from pBluescript plasmid (Stratagene/Agilent Technologies) is first amplified by PCR using forward primer 5′-AAAAGAATTCCTCAGCGACGCAG GGGACCTGCAGG and reverse primer 5′- AAAACTCGAGTGCCGTTG TAACCGGTCATC. The PCR product was then digested with *Eco*RI and *Xho*I and subsequently ligated to the dsDNA-construct handles.

Construction of DNA hairpin handles

To create biotin- and digoxigenin-labeled handles, a 1.2-kb fragment of pBluescript plasmid (Stratagene/Agilent Technologies) is amplified by PCR using forward primer 5′-GACCGAGATAGGGTTGAGTG and reverse primer 5′-CAGGGTCGGAACAGGAGAGC in the presence of biotin-16-dUTP and digoxigenin-11-dUTP (both from Roche Diagnostics), respectively. These handles are then digested with *Bam*HI and *Not*I, respectively, and subsequently ligated to double-stranded spacer segments that have been previously assembled by annealing the appropriate oligos (Fig. S1 and Supporting Material). The resulting products form the upper and lower arms of the hairpin, respectively (Figs. 1 *A* and S1). All oligonucleotides are obtained from Biolegio B.V., Nijmegen, The Netherlands; oligonucleotide sequences are provided in the Supporting Material.

Assembly of a fully tetherable DNA hairpin

To form the core of the DNA hairpin, a 1.0 kb fragment from pEAV211 plasmid (kindly provided by Dr. Aartjan te Velthuis, Leiden University Medical Centre, Leiden, The Netherlands) is first amplified by PCR using forward primer 5′-CTCCTGTGTGGTCTCGTTGCGAAGTAGTTATTAG CCACCCAG and reverse primer 5′-GATAATACCGGGTCTCCTAGGA GAACTTTAAAAGTGCTCATCATTG. This PCR product is then digested with *Bsa*I and ligated to a 42-base oligonucleotide (Fig. S1, *green*) to close the hairpin (Figs. 1 *A* and S1). The upper and lower handles (including spacers (see preceding subsection)) are annealed together to form a short (50 bp) stem with a *Bsa*I overhang. This stem is then ligated to the other side of the 1.1 kb pEAV211 fragment. The sequence of the single-stranded DNA (ssDNA) part of the handle and the first 50 nucleotides of the stem (bold) is given by 5′-CCAAGTCATTCTGAGAATAGTGTATGCGGCGA CCGAGTTGCTCTTGCCTTTTTTTTTTT**ATGCTCTTTACAACCGGTT GACTGCTTCAGGGGTCGATCCCGCTTTGTAC**-3′. All oligonucleotides were obtained from Biolegio B.V. (Supporting Material).

Bead tethering and buffer conditions in the flow cell

After the flow cell is mounted onto the MT microscope, we flush in buffer A (10 mM Tris-HCl, pH 8, 0.5 mM EDTA, 150 mM NaCl, and 0.01% Tween-20). Then, we flush in 20 μL antidigoxigenin (1 g/L in buffer A) and incubate for 30 min. Subsequently, we rinse the flow cell with 200 μL of buffer A and passivate it with BlockAid (20 μL, Life Technologies) via a 30 min incubation. To remove any excess BlockAid, we then thoroughly rinse the flow cell again with buffer A. In parallel, we mix 10 μL of a 0.1 ng/μL DNA hairpin or dsDNA-construct stock solution with 10 μL of twice-washed MyOne superparamagnetic beads resuspended in buffer A and incubate for 10 min. Subsequently, this solution containing hairpin-tethered beads is flushed into the flow cell, where it is incubated for 30 min. Finally, we again thoroughly rinse the flow cell with buffer A. To remove any nonspecifically attached beads, we scan the magnets above the flow cell from its inlet to its outlet, applying high force and rotations as necessary. Rinsing the flow cell subsequently with buffer A removes the remaining nonspecifically attached beads.

For the experiments in which we observe the effect of dTTP (Sigma Aldrich, Zwijndrecht, The Netherlands) on the hopping transition of the hairpin (see Figs. 4 and 5), we exchange buffer A from the flow cell with buffer B, which contains 20 mM Tris-HCl, pH 7.5, 50 mM NaCl, 7 mM $MgCl_2$, 3 mM EDTA, 0.01% Tween-20, and varying concentrations of dTTP.

Noise due to thermal fluctuations

Thermal noise arises from the fact that the DNA-tethered bead experiences Brownian fluctuations in a (approximately) harmonic potential (35–37). The stiffness of the system in the z-direction (which is the relevant dimension in most MT assays) can be expressed as (36)

$$k_z = \frac{\partial F(\langle L_{\text{ext}}\rangle)}{\partial \langle L_{\text{ext}}\rangle} = \frac{k_B T}{2 L_P L_0} \times \left(2 + \left(1 - \frac{\langle L_{\text{ext}}\rangle}{L_0}\right)^{-3}\right), \quad (1)$$

where we have used the inextensible wormlike chain model (38) to define the restoring force that acts on the tether. In this expression, $\langle L_{\text{ext}}\rangle$ is the average extension of the DNA tether, L_P is the persistence length of the DNA tether, L_0 is the contour length of the DNA tether, k_B is Boltzmann's constant, and T is the absolute temperature. From Eq. 1, we observe that both L_0 and L_P (both of which differ for single-stranded versus double-stranded tethers) will significantly influence the system's stiffness along the z axis. As the variance of the thermally induced fluctuations in the z-direction can be expressed as (Fig. 1 *B*)

$$\langle \delta z^2 \rangle = \frac{k_B T}{k_z}, \quad (2)$$

the stiffness, k_z, will determine the magnitude of the noise. This remains correct despite the fact that Eq. 2. should only be viewed as an approximation, as the potential is not strictly harmonic (39) in the z-direction (40). Interestingly, combining Eq. 1. with Eq. 2. reveals that $\langle \delta z^2 \rangle$ is independent of the bead radius employed (the same does not hold true for the timescale of the fluctuations, however, as detailed in the next section). The variance of the bead position is by definition the integral from 0 to ∞ of the power spectral density, $S_z(f)$, of the system. If the detection system is not capable of fully capturing the system's complete bandwidth, e.g., as a result of low camera acquisition rates (36,41,42), the expression for the integral of the power spectrum must be adapted to (6)

$$\langle \delta z^2 \rangle = \int_0^{B_{\text{eq}}} S_z(f) df = \frac{2 k_B T}{\pi k_z} \arctan\left(\frac{B_{\text{eq}}}{f_{c,z}}\right), \quad (3)$$

where B_{eq} is the equivalent noise bandwidth, i.e., the bandwidth of a fictitious rectangular window low-pass filter that provides the same noise power as the measurement system under study, and $f_{c,z}$ is the corner frequency of the system along the z axis.

Characteristic timescale of *z*-fluctuations in MT

To fully appreciate the impact of thermal noise on experimental measurements, one must also evaluate the response time of the system. To do so, we start from the bead's equation of motion (assuming that inertial contributions are negligible) (40):

$$\gamma_0 \times \dot{z}(t) + k_z \times z(t) + F_{\text{WLC}} = F_{\text{therm}} + F - F_{\text{grav}}, \quad (4)$$

where γ_0 is the friction coefficient (which is equal to $6\pi\eta R$, where η is the viscosity, provided the bead is sufficiently far from the surface), F_{WLC} is the restoring force on the nucleic acid tether, F_{therm} is the thermal (or Langevin)

force on the bead that results from random collisions with water molecules, and F_{grav} is the gravitational force on the bead. From Eq. 4, we can compute the theoretical power spectrum density of the Brownian fluctuations and deduce the associated system correlation time:

$$t_{c,z} = \frac{1}{2\pi f_{c,z}} = \frac{\gamma_0}{k_z}. \quad (5)$$

Given that γ_0 scales linearly with R, Eq. 5. implies that to maximize bandwidth, one should use the smallest bead possible. Maximizing k_z furthermore implies that the shortest possible tether should be employed (Eq. 1). Nonetheless, there is a limitation to this approach, as the viscous drag experienced by a bead increases as it approaches the flow-cell surface according to Faxén's law (43),

$$\gamma_{Faxén,z}(\langle z\rangle) = \frac{\gamma_0}{\left[1 - \frac{9}{8}\left(\frac{R}{\langle z\rangle}\right) + \frac{1}{2}\left(\frac{R}{\langle z\rangle}\right)^3 - \frac{57}{100}\left(\frac{R}{\langle z\rangle}\right)^4 + \frac{1}{5}\left(\frac{R}{\langle z\rangle}\right)^5 + \frac{7}{200}\left(\frac{R}{\langle z\rangle}\right)^{11} - \frac{1}{25}\left(\frac{R}{\langle z\rangle}\right)^{12}\right]}, \quad (6)$$

where $\langle z\rangle = L_{ext} + R$.

We numerically evaluate the standard deviation of the noise, δz (Eq. 3 and Fig. 1 *B*), and $t_{c,z}$ (Eq. 5 and Fig. 1 *C*) for the bead-tether system at 100 Hz equivalent noise bandwidth, taking into account the increased drag in the vicinity of the flow-cell surface. We observe a dependence on the stiffness and on the length of the tether; for example, for a tether of the same end-to-end extension, dsDNA (Fig. 1, *B* and *C*, *red line*) provides a higher bandwidth than ssDNA (Fig. 1, *B* and *C*, *black line*). Furthermore, we perform numerical simulations of tethered magnetic beads in an MT assay (Supporting Material and Figs. S4 and S5, *B–D*), as described previously (40). This allows us to examine the fluctuations in z for different tether conditions. In the Results section, we compare these findings to experimental results.

Other sources of noise

Instrumental noise includes contributions from both tracking errors in the determination of the bead position (26) and mechanical drift. We can quantify the magnitude of these noise sources by tracking beads that are stably attached to the surface and do not undergo Brownian motion. Tracking noise results from the fact that the determination of the bead position from camera images is subject to measurement uncertainty. Tracking noise is uncorrelated from frame to frame (26) and has a variance, σ^2_{track}, that is approximately constant for a given light intensity. By increasing the number of sampled positions, N, and averaging over them, the contribution of tracking noise to the mean positional uncertainty may be decreased according to

$$\sqrt{\sigma^2_{track}/N}. \quad (7)$$

The expression in Eq. 7 implies that a higher acquisition speed will permit a significant reduction in tracking noise at a given bandwidth, provided the frame-to-frame tracking error, σ_{track}, can be kept constant. Keeping σ_{track} constant in particular requires maintaining the illumination intensity per frame constant, which typically is the limiting factor for high acquisition speeds. Finally, an additional source of noise arises from position drift in the experimental apparatus, e.g., from thermal expansion or mechanical vibrations. For the longest measurements, drift will be the limiting factor, given that the contributions from all other sources of noise can be reduced by averaging.

RESULTS AND DISCUSSION

Spatiotemporal resolution for surface-melted beads with LED- and laser-based illumination

We first quantify the spatiotemporal resolution of our instrument along the z axis using beads that are stably attached to the flow-cell surface by melting (Materials and Methods, Fig. 2 *A*). To reduce the influence of mechanical drift, we subtract the position of one such surface-melted bead from an identical second bead. For quantification of the spatiotemporal resolution, we compute the Allan deviation (AD) (44,45), which is defined as one-half the average difference in position between adjacent intervals of length τ averaged over all intervals of length τ. This provides a measure of the spatial resolution for a measurement of duration τ (28,44,45). As detailed in the Supporting Material, an important consideration in achieving optimal spatiotemporal resolution is the available light intensity for sample illumination (Fig. S3): at low light intensities, the tracking noise will become the limiting factor; conversely, at saturating illumination intensities, the lack of contrast between the rings in the diffraction pattern will become limiting. For example, for a 3-μm-diameter surface-melted bead tracked at 500 Hz under LED-based illumination, we achieve an optimal resolution of 0.014 nm at 4 s using 175 gray levels (for an available total of 256 gray levels) (Fig. S3 *B*). Indeed, a $1/\sqrt{I}$ dependence between the value of the AD at 1 s and the illumination intensity is observed (Fig. S3 *F*, *red line*) before camera saturation, consistent with the tracking error being shot-noise limited at low light intensities. Additionally, the achievable spatiotemporal resolution depends on the type of surface-melted bead employed (Fig. S2 *E*): we find that larger beads provide better spatial resolution for a given measurement duration and light intensity, with the resolution improving approximately as R_{bead}, consistent with predictions from basic Mie theory for the scattered light intensity (Fig. S2 *G* and Supporting Material). For example, for 2.8-μm-diameter M270 beads (Fig. S3 *E*, *blue line*), the AD equals 0.1 nm and 0.02 nm over measurement times of 0.01 s and 1 s, respectively; the corresponding values obtained for 1.0-μm-diameter MyOne beads are limited to 0.4 nm and 0.04 nm (Fig. S3 *E*, *dashed blue line*).

Using such optimized conditions, we compare the AD for surface-melted beads under different illumination conditions provided by either a high-power fiber-coupled LED

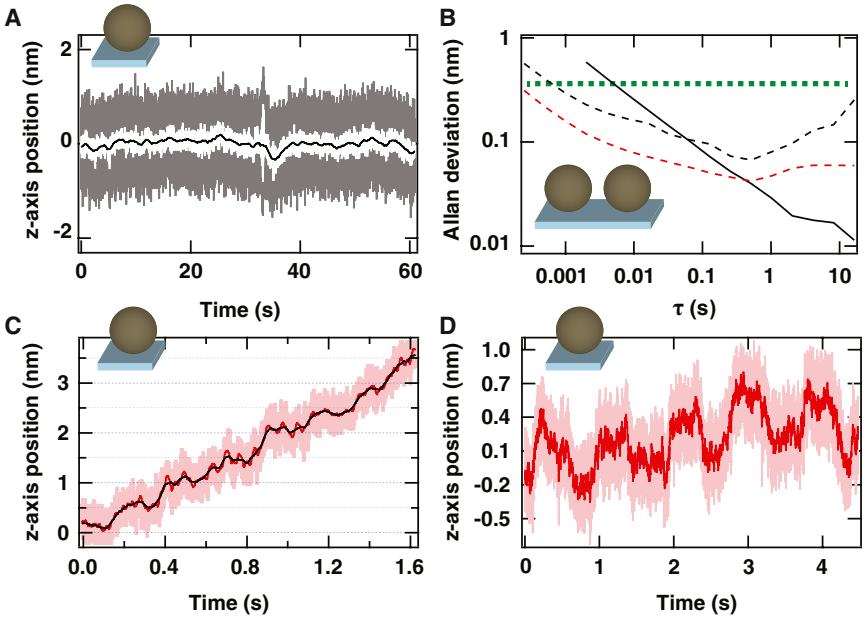

FIGURE 2 Spatiotemporal resolution for surface-melted beads. (*A*) Typical trace of the tracked position along the *z*-coordinate of a surface-melted latex bead (1.5 μm diameter). This trace does not include subtraction of the reference-bead position. Laser illumination is employed, and real-time tracking is performed at 4 kHz. Gray line, raw data; white line, data boxcar filtered at 10 ms; black line, data boxcar filtered at 1 s. (*B*) The ADs for 1.5-μm-diameter surface-melted latex beads under different types of illumination: laser illumination coupled to an acquisition frequency of 4 kHz (*black* and *red dashed lines*) and a high-power fiber-coupled LED illumination coupled to an acquisition frequency of 500 Hz (*black solid line*). All data sets were measured at an illumination intensity corresponding to 150 gray levels. The reference-bead position has been subtracted from that of the surface-melted beads before computation of the AD for the black dashed and solid lines. The red dashed line is the AD of the trace in (*A*), for which the reference-bead position has not been subtracted. The horizontal green dashed line in (*B*) represents the distance between basepairs of dsDNA, 0.34 nm. (*C*) Resolving 0.5 nm steps every 0.25 s using a 3 μm surface-melted latex bead. The raw data (at 6 kHz acquisition frequency), data smoothed at 100 Hz, and data smoothed at 20 Hz are represented in light red, red, and black, respectively. The inset is a zoom of the steps. (*D*) Resolving 0.3 nm steps every 0.5 s with a 2.8-μm-diameter surface-melted M270 magnetic bead. The color code is identical to that in (*C*). In both (*C*) and (*D*), a laser is used to illuminate the field of view, resulting in an intensity of 150 gray levels on the camera. To see this figure in color, go online.

(with acquisition at 500 Hz; Fig. 2 *B*, *black solid line*) or a rapidly modulated laser diode (with acquisition at 4 kHz; Fig. 2 *B*, *black dashed line*). Broadly speaking, the AD decreases for short τ (up to ~1 s) approximately as $1/\sqrt{\tau}$ (Fig. 2 *B*, *black dashed line*). In this so-called shot-noise limit, the AD can be thought of as the standard error of the mean of the bead's position, a quantity that decreases with the square root of the number of independent measurements. However, this decrease of the AD is halted at longer τ (1–10 s; Fig. 2 *B*), and subsequently, the AD is seen to increase. This increase in the AD indicates that drift in the position measurement starts to dominate the noise. For both types of illumination examined here, we observe that the frame-to-frame resolution (which can be read off from the value of the AD at the smallest available τ) is identical: hence, the nature of the source does not affect the tracking resolution. At longer time intervals, we observe an AD of 0.57 nm at 0.002 s and 0.02 nm at 1 s for the case of LED-based illumination (Fig. 2 *B*, *black solid line*), and an AD of 0.22 nm at 0.002 s for the case of laser-based illumination (Fig. 2 *B*, *black dashed line*). Thus, the use of laser-based illumination yields a 2.6-fold improvement in the achievable spatial resolution at short timescales compared to LED illumination. The improvement is in excellent agreement with the expected $1/\sqrt{N}$ scaling (Eq. 7) (Fig. S3 *E*), which would imply a $\sqrt{4000\ \mathrm{Hz}/500\ \mathrm{Hz}} = 2.8$ -fold decrease. Subtracting a reference-bead position suppresses most of the mechanical drift in the AD but adds the uncorrelated tracking noise of the reference bead to the AD of the bead of interest. Therefore, we observe, for the laser-based illumination, a reduced AD for the position signal of a single bead in the absence of reference-bead subtraction (Fig. 2 *B*, *red dashed line*) compared to with reference-bead subtraction (Fig. 2 *B*, *black dashed line*), which yields a best spatiotemporal resolution of 0.04 nm over 0.5 s. We do note that drift sets in slightly earlier for laser-based illumination compared to LED-based illumination, as the AD for the former is observed to increase for $\tau \geq 0.1$ s (Fig. 2 *B*). The drift in the laser-based illumination on slightly shorter timescales compared to LED-based illumination likely results from either residual speckle that is not eliminated by rapid modulation of the laser wavelength (Materials and Methods), or from the disruptions in illumination caused by the coupling of imperfections in optical elements to mechanical drift (Materials and Methods). Importantly, however, the AD still remains far below basepair resolution at longer timescales (<0.1 nm at 1 s). The improved resolution achieved using laser illumination is particularly useful when one employs small (e.g., 1-μm-diameter MyOne beads), as it can compensate for the lower spatial resolution that is otherwise achieved with such beads.

To further test and demonstrate the capabilities of laser-based illumination for high spatiotemporal resolution measurements, we generate steplike motion using the piezo stage onto which the microscope objective is mounted and track the relative motion of a single surface-melted bead

(since reference-bead-based correction for mechanical drift is not possible for steps that are generated by moving the objective). As shown in Fig. 2 *C*, we can resolve 0.5 nm steps in the raw data at 6 kHz (*light red region*) as the piezo stage is moved in steps of 0.5 nm every 0.25 s. Boxcar filtering at 100 Hz (Fig. 2 *C*, *red line*) or 20 Hz (Fig. 2 *C*, *black line*) defines these steps more clearly. In addition, we resolve 0.3 nm back-and-forth steps (comparable to the 0.34 nm separation between DNA basepairs) when the stage is modulated at a slightly longer period of 1 s (Fig. 2 *D*). These steps are well defined in the raw data acquired at 6 kHz (Fig. 2 *D*, *light red region*) and further highlighted using boxcar filtering at 100 Hz (Fig. 2 *D*, *red region*).

The use of small beads with short double-stranded tethers provides high spatiotemporal resolution

We now characterize our instrument's spatial resolution for beads tethered to either a dsDNA or to a DNA hairpin that includes a partially single-stranded handle (Figs. 3, S4, and S5). As for the surface-melted beads described above, we assay the system's spatiotemporal resolution by resolving piezo stepping motion along the z axis and by employing the AD to characterize a bead-tether's response over a range of timescales.

We first investigate our ability to resolve stepping motion along the z axis generated by the piezo stage on a MyOne magnetic bead tethered to a 1.9 kbp dsDNA construct (contour length ~0.65 μm) under an applied force of 18 pN (Fig. 3, *A* and *B*). As above, in this assay, it is not possible to correct for mechanical drift using reference-bead subtraction, as steps are generated by moving the objective along the z axis. To generate the steps, we use a square-wave function with an amplitude of either 1 nm (Fig. 3 *A*) or 0.5 nm (Fig. 3 *B*) and a period of ~0.75 s. For both cases, we acquire the data under laser-based illumination at 8 kHz with boxcar filtering to 100 Hz (Fig. 3, *A* and *B*, *red*) or 10 Hz (Fig. 3, *A* and *B*, *black*) and are able to resolve the steps generated by the piezo. In similar conditions, Seidel and co-workers resolved similarly sized piezo step motion using an incoherent light source and measured an AD of 0.3 nm over 0.01 s (29), comparable to our measurement of 0.4 nm over 0.01 s.

To further quantify the spatiotemporal resolution achievable on dsDNA-tethered beads, we coplot the AD signals (Fig. 3 *C*) for laser-based illumination (at 8 kHz acquisition frequency) (Fig. 3 *A*) versus LED-based illumination (at 500 Hz acquisition frequency; raw data trace not shown). In our experimental conditions, e.g., a 1.9 kbp dsDNA-tethered bead and an applied force of 18 pN (Fig. 1 *B*), we expect the tracking noise to dominate the intrinsic thermal noise due to Brownian fluctuations (Figs. S3 *F* and S4 *A*, *blue dashed line*). For an object that experiences a harmonic energy potential, as a tethered magnetic bead subjected to force does, the AD value increases with τ until τ equals 1.89-fold the system correlation time and subsequently

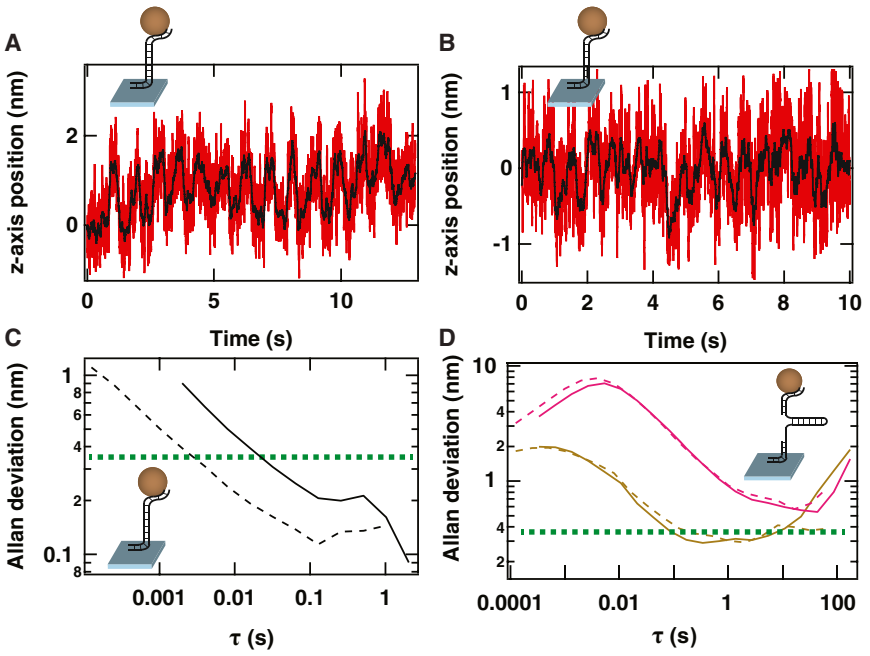

FIGURE 3 Spatiotemporal resolution for dsDNA- and hairpin-tethered magnetic beads. (*A*) Resolving 1.0 nm steps along the z axis with a 1.9 kbp dsDNA tethered to a MyOne bead, under a force of 18 pN. The steps are performed by the piezo stage every 0.25 s. (*B*) Resolving 0.5 nm steps along the z axis with a 1.9 kbp dsDNA tethered to a MyOne bead, under a force of 18 pN. The steps result from the square-wave motion of the piezo stage with a period of 0.75 s. In (*A*) and (*B*), the raw data have been acquired with a laser-based illumination at an acquisition frequency of 8 kHz and subsequently boxcar filtered at 100 Hz (*red*) and 10 Hz (*black*). (*C*) The AD of the z-position for a 1.9 kbp dsDNA tethered MyOne bead at 18 pN force, illuminated either by a laser-based illumination (*dashed line*; 8 kHz acquisition frequency (*A*)) or an LED-based illumination (*solid line*; 500 Hz acquisition frequency). (*D*) The AD of the x (*pink lines*) and z (*brown lines*) positions for a hairpin tethered to a MyOne bead under ~12 pN of force (closed hairpin). Illumination is provided either by a high-power fiber-coupled LED-based illumination (*solid lines*), in which case 100× magnification is employed and real-time tracking is performed at an acquisition frequency of 3 kHz, or by laser-based illumination (*dashed lines*), in which case 200× magnification is employed and real-time tracking is performed at an acquisition frequency of 8 kHz. In both cases, the number of gray levels is set to 150. The horizontal green dashed line in (*C*) and (*D*) represents the DNA basepair distance, 0.34 nm. To see this figure in color, go online.

decreases for larger τ proportional to $\tau^{-1/2}$ until drift becomes the dominant source of noise for even longer τ (44,45). However, here, we do not observe a peak in the AD signal for either case (Fig. 3 *C*). The absence of the AD peak is expected for two reasons. First, as stated above, the tracking noise is limiting the resolution in this experiment. Second, the minimal sampling time, 125 μs (the inverse of the 8 kHz acquisition frequency employed) far exceeds the predicted correlation time of ~4×10^{-7} s (Eq. 5). For these dsDNA-tethered beads, we also observe a clear improvement using laser-based illumination with an acquisition frequency of 8 kHz (Fig. 3 *C*, *dashed black line*) compared to LED-based illumination with an acquisition frequency of 500 Hz (Fig. 3 *C*, *solid black line*). For a measurement interval of 0.008 s, for example, we obtain an AD of 0.23 nm using laser-based illumination, twofold lower than the AD of 0.5 nm achievable using LED-based illumination (Fig. 3 *C*). We observe similar results from a numerical simulation (Supporting Material and Fig. S4 *C*) with the same parameter values (2 kbp, $L_P = 50$ nm, 18 pN applied force, 1-μm-diameter bead). Thus, both experimental results and numerical simulations indicate that by averaging the tracking noise, laser-based illumination provides improved spatiotemporal resolution over LED-based illumination.

We next quantify the spatiotemporal resolution achievable for a magnetic bead tethered to a DNA hairpin (Figs. 1 *A* and S4 *A*), a common tether in high-resolution single-molecule force spectroscopy experiments of enzymatic activity (22,28,46–51). We note first that our calculations (Fig. 1, *B* and *C*, and Eq. 3) indicate that the spatiotemporal resolution achievable for tethered ssDNA (Fig. 1 *B*, *black line*) is inferior to that for dsDNA of comparable length (Fig. 1 *B*, *red line*). For example, for tethers with an end-to-end distance of 0.65 μm, the expected spatial resolution values in z are 2 nm and 5 nm for dsDNA and ssDNA, respectively (Fig. 1 *B*). These results lead us to predict a decreased spatial resolution for a tethered DNA hairpin (with its partially ssDNA handle; see Fig. 1 *A*) compared to a fully dsDNA tether. In line with these expectations, we measure an AD of 1 nm over 0.01 s (Fig. 3 *D*, *brown solid lines*) for a hairpin with a short, 200 nm handle and an AD of 0.25 nm over 0.008 s for dsDNA with a length of 650 nm (Fig. 3 *C*, *black solid line*). In other words, the reduction in stiffness that results from the addition of a 40-nucleotide ssDNA sequence in the handle exceeds even the gain in stiffness upon reduction of the tether length (from 650 nm for the dsDNA tether to 200 nm for the hairpin handles). Therefore, for closed-hairpin tethers with a partially ssDNA handle, the resolution is limited by the noise level that results from thermal fluctuations of the ssDNA region. This is confirmed by the fact that for such tethers we observe no difference between laser-based (Fig. 3 *D*, *dashed lines*) or LED-based (Fig. 3 *D*, *solid lines*) illumination at either 200× or 100× magnification, respectively: both illumination protocols provide at best an AD of 0.3 nm at 1 s bandwidth along x (Fig. 3 *D*, *pink lines*) or z (Fig. 3 *D*, *brown lines*). As expected, thermal fluctuations also dominate the observed fluctuations for open DNA hairpins, as confirmed by both simulations (Supporting Material and Fig. S5, *B–D*) and experiments (Fig. S5 *E*).

We further observe several other aspects of the stiffness of DNA hairpins. To start, we observe that the experimentally measured z-fluctuations for a closed DNA hairpin with a short handle are equal to those predicted by Eqs. 3 and 5 for a 200-nm-long, fully ssDNA tether (see the Supporting Material). This leads us to conclude that dynamics of the handle dominate the overall response of the hairpin. In line with this expectation, calculations predict a larger standard deviation in the bead position along the z axis (Fig. 1 *B*) and a reduced characteristic time (Fig. 1 *C*) for a hairpin with a longer (700 nm) handle. This observation is confirmed experimentally: we measure an AD of 1 nm over 0.01 s, and a characteristic time of ~0.25 ms, for a hairpin attached via a 200 nm handle, and we measure an AD of 3 nm over 0.01 s, and a characteristic time of ~0.4 ms, for a hairpin attached via a 700 nm handle (Fig. S4 *F*). As expected, attaching a magnetic bead with a larger diameter to a DNA hairpin also results in a longer correlation time: we measure a characteristic time of ~0.25 ms from the peak in the AD for a 1-μm-diameter bead and, similarly, a characteristic time of ~1.8 ms for a 2.8-μm-diameter bead (Eqs. 5 and 6 and Fig. S4 *E*).

Both DNA-hairpin-tethered beads and dsDNA-tethered beads provide results that are in agreement with the calculations (Fig. 1, *A* and *B*) and the numerical simulations (Figs. S4 and S5, *B–E*) and therefore suggest that our simple theoretical framework offers a reasonable estimate of the resolution achievable with MT for a particular set of experimental conditions. We demonstrate here that a laser-based illumination together with high acquisition frequency provides the conditions for high-spatiotemporal-resolution MT, given that the limiting noise arises from the tracking noise.

Monitoring hairpin hopping using high-spatiotemporal-resolution MT

Having characterized the spatiotemporal aspect of our high-resolution MT, we demonstrate its utility by implementing a series of biophysical experiments on conformational transitions of tethered hairpins. In this series of measurements, we apply a force of ~12 pN to a short-handled DNA hairpin tethered to a MyOne bead (see Materials and Methods) and record its position under laser illumination at an acquisition frequency of 8 kHz for hundreds of seconds (Fig. 4 *A*). The extension-versus-time traces reveal two stable positions for forces in the range 11–13 pN (Fig. 4 *B*). Between these two stable positions, we observe rapid, stochastic transitions that have dwell times on the order of 1–100 ms (Fig. 4 *C*). We interpret the hopping transitions as thermally driven

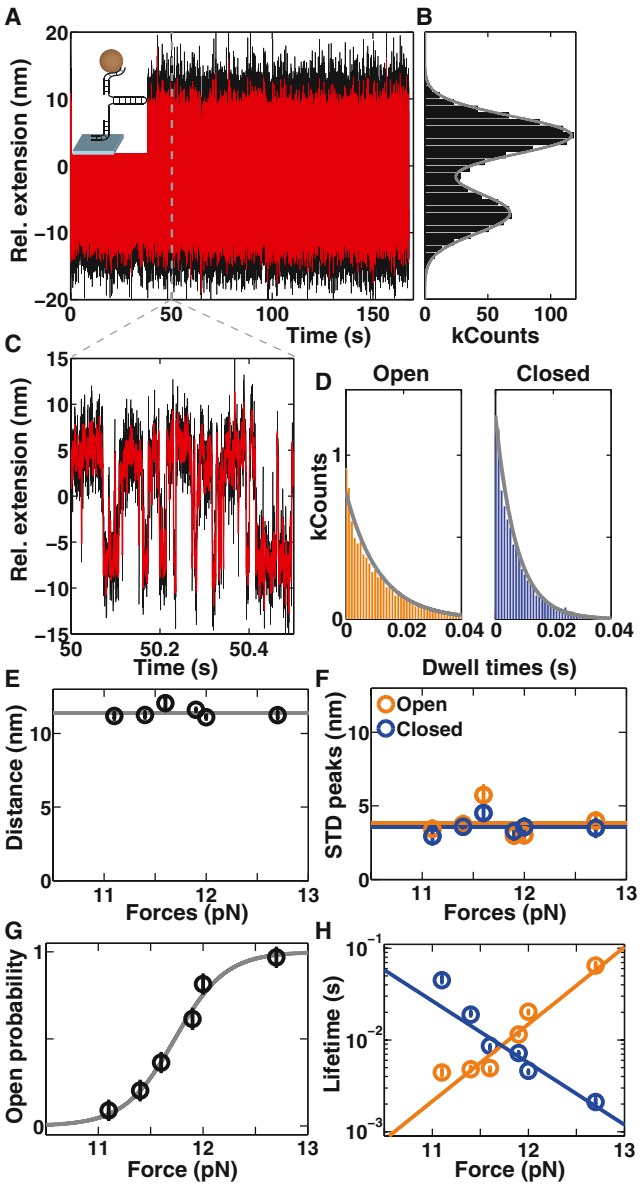

FIGURE 4 Resolving fast hairpin opening and closing transitions. The data presented are from a single DNA hairpin with a 1052 bp stem and a 40 nucleotide ssDNA handle (Fig. 1 *A* and Materials and Methods) tethered between a flow-cell surface and a MyOne bead. (*A*) Time trace of the extension at 11.9 pN stretching force. Raw data were recorded at 8 kHz (*black*) with laser illumination and a resulting intensity of 150 gray levels on the camera. The data were subsequently filtered at 1 kHz (*red*). (*B*) Histogram of the extension data from (*A*) (*black*; the bin size is 1 nm) and fit to a double Gaussian (*gray line*). (*C*) Zoom of a segment of the extension time trace. The zoomed-in region is indicated by the dashed gray lines in (*A*). The same color code is employed as in (*A*). (*D*) Distribution of dwell times in the up/open (*orange*) and down/closed (*blue*) states determined from the 1 kHz filtered data from (*A*). Bin size is 1 ms. Gray lines are exponential functions determined from a maximum-likelihood fit to the data with $\tau_{open} = 11.5 \pm 0.3$ ms and $\tau_{closed} = 7.2 \pm 0.2$ ms. (*E*) Distance between the open- and closed-state peaks as a function of applied stretching force. Averaged over all points, the mean is 11.4 ± 0.4 nm (*solid line*). (*F*) Standard deviation of the open- (*orange*) and closed-state (*blue*) peaks from double Gaussian fits. The averages of the standard deviations are 3.8 ± 1.0 and 3.6 ± 0.5 nm, respectively (as indicated by the solid lines of the same color). (*G*) Fraction of time spent in the open state as a function of applied force. The gray line is a fit (reduced $\chi^2 = 0.71$) of a two-state model, indicating a transition force, $F_{1/2} = 11.7$ pN. Data points and error bars in panels (*E*)–(*G*) are the mean and standard deviations of 3 traces recorded on the same hairpin. Errorbars for some points are smaller than the symbols. (*H*) Lifetimes of the open (*orange*) and closed (*blue*) states as a function of applied force. Lifetimes were determined from maximum-likelihood fits to the dwell-time distributions in (*D*). Solid lines are exponential fits of the form $\tau_{o/c}(F) = \tau_{o/c}(0) \times \exp(\Delta x_{o/c} \times F/k_BT)$ with $\tau_{open}(0) = 1.85$ fs, $\tau_{closed}(0) = 1.75$ ms, $\Delta x_{open} = 7.70$ nm, and $\Delta x_{closed} = -6.68$ nm. Error bars indicate the 95% confidence intervals of the maximum-likelihood exponential fits to the dwell-time distributions. To see this figure in color, go online.

transitions between a closed and a partially open conformation of the hairpin. Notably, the observed extension change is much smaller than the extension change of ~1000 nm observed for full opening of the hairpin, which occurs at forces of ~16 pN under the buffer conditions employed. Therefore, we assign the transition to the opening of a short, likely AT-rich, segment of the hairpin.

To further quantify the data, we determine the dwell-time distributions in the open and closed states (Fig. 4 *D*) by assigning an extension threshold at the position of the minimum between the two Gaussians that correspond to the open and closed states (Fig. 4 *B*). The dwell times are exponentially distributed (Fig. 4 *D*), as is expected and routinely observed for thermally activated, stochastic barrier-crossing events (for reviews, see, e.g., Hänggi et al. (52) and Bustamante et al. (53)). Recording similar traces on the same hairpin at slightly different applied stretching forces, we find that neither the distance between the two peaks nor their standard deviations change significantly with force over the range investigated (Fig. 4, *E* and *F*). The fraction of the time spent in the open state, however, changes rapidly with applied force, consistent with a two-state model with a transition force of $F_{1/2} = 11.7$ pN (Fig. 4 *G*). Finally, the lifetimes of the open and closed states, determined from exponential fits of the dwell-time distributions, depend exponentially on the applied stretching force (Fig. 4 *H*). From the distance between the open and closed states of 11.4 ± 0.4 nm, we estimate that the observed transitions correspond to the opening of a 9- to 11-bp-long segment (taking into account the 2 nm width of the DNA helix and assuming an extension of 0.5 nm per nucleotide (28,54,55)). The observed unfolding force lies well within the range of forces observed previously for short hairpins (54,56). We observe dwell times of the open and closed states with lifetimes in the range of ~10 ms, with values down to 2 ms, highlighting the temporal resolution of our instrument (Fig. 4 *H*). The mean lifetimes have been fitted using the Bell model of rupture bonds (57) following the approach taken by several single-molecule studies of DNA- or RNA-hairpin unfolding measurements (53,54,56,58). In addition, the characteristic time in the range of 10 ms observed in our measurement is consistent

with previous observations of short, ~10-bp-long, hairpins (54). In summary, our observation of the opening and closing transitions of a short, ~10 bp, segment of our hairpin highlights the ability of our current MT implementation to record long (>100 s) and stable time traces observing macromolecular transitions at approximately nanometer lengthscales and approximately millisecond timescales.

dTTP presence in the buffer modifies the behavior of the hairpin hopping

Having demonstrated that our assay can monitor hairpin opening and closing transitions with high precision over extended periods of time, we tested whether it could be used to sense the presence of nucleotides in solution. Recently, it was shown that hairpin transitions can be used to sensitively probe the ionic environment (59,60) and might even provide a platform for single-molecule sequencing (47). Studies of nucleic-acid-dependent molecular motors typically require high concentrations of nucleoside triphosphates (NTPs) in solution to power the enzymes: this is the case for helicases (61,62), ribosomes (63), and polymerases (62,64–66); in the latter case, the nucleotides also serve as the building blocks for the nascent nucleic acid product. To test the effect of high concentrations of NTPs in the absence of any enzymes on the hairpin opening dynamics and to investigate whether we can detect binding of NTPs to the DNA in the open state, we recorded traces at a constant force, ~12 pN, close to the characteristic transition force, $F_{1/2}$ (Fig. 4 *G*), at different dTTP concentrations.

From our experiments, we determined that neither the distance between the peaks in the extension histogram corresponding to the open and closed states nor the width of the peaks changed significantly with dTTP concentration (Fig. 5 *A*). In contrast, addition of dTTP shifted the equilibrium to the open state (Fig. 5 *B*). The observed change in the fraction of time spent in the open state was reasonably well described by a simple binding isotherm model (Fig. 5 *A*, *solid line*), with a midpoint concentration of ~90 μM dTTP. In addition, increasing dTTP concentration increased the lifetime in the open state and decreased—to a lesser extent—the lifetime of the closed state (Fig. 5, *C* and *D*). These observations suggest that the presence of dTTP in the buffer stabilizes the open state with respect to the closed state. The binding isotherm (Fig. 5 *B*) implies that the free-energy change upon addition of dTTP is proportional to the logarithm of the dTTP concentration; i.e., the logarithm of the dTTP concentration plays a role analogous to the force in the force-dependent measurements (Fig. 4). We note that even though all data in Fig. 5 were recorded at the same force, the force is still available as a control parameter that makes it possible to tune the sensitivity of the hairpin assay in a desired range. Our data indicate that dTTP interactions with the hairpin stabilize the open state, with an apparent binding midpoint of 92 μM. It appears plausible that dTTP molecules in solution would interact via Watson-Crick base-pairing with adenine bases in the hairpin that are accessible in the open state but sequestered in the (double-stranded) closed state. However, electrostatic or ionic effects might also play a role. Although a complete dissection and attribution of the observed interactions will require more extensive measurements with a variety of hairpin sequences, our results indicate that the observation of hairpin opening and closing transitions in high-resolution MT have the potential to serve as molecular sensors of tunable sensitivity.

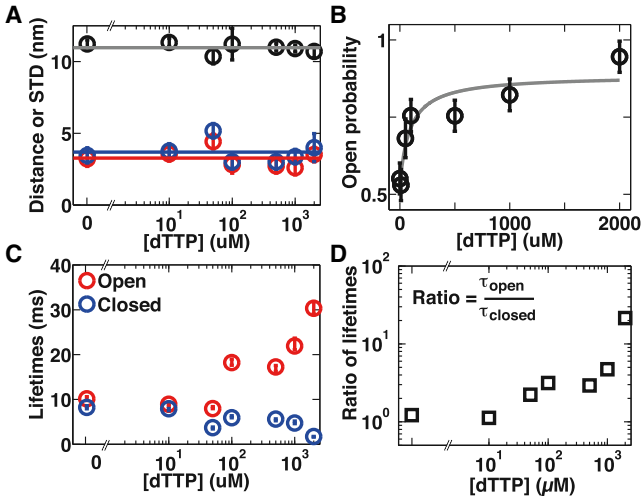

FIGURE 5 The hairpin opening transition acts as a molecular sensor for dTTP. The data presented are for the same bead-tether combination and illumination settings as in Fig. 4, obtained under a constant force of 11.8 pN. (*A*) The distance between the open and closed states (*black circles*) and the standard deviations of the peaks corresponding to the open (*red circles*) and closed (*blue circles*) states as a function of dTTP concentration. Distances and standard deviations were determined from double Gaussian fits similar to that in Fig. 4 *B*. Data points and error bars here and in (*B*) are the mean ± SD values of three traces recorded under identical conditions. Error bars for some points are smaller than the symbols. Lines are the mean values (distance = 10.9 ± 0.4 nm; $\langle \mathrm{STD}_{\mathrm{open}} \rangle$ = 3.3 ± 0.7 nm; $\langle \mathrm{STD}_{\mathrm{closed}} \rangle$ = 3.7 ± 0.7 nm) of the corresponding quantities, averaged over all dTTP concentrations. (*B*) The fraction of time spent in the open state as a function of dTTP concentration. The data were fit (reduced $\chi^2 = 1.27$) to a binding isotherm (*gray line*) of the form $p_{\mathrm{open}} = c_1 + c_2 \times [\mathrm{dTTP}]/([\mathrm{dTTP}] + K)$, with fitted constants $c_1 = 0.53$ and $c_2 = 0.35$ and binding constant $K = 92$ μM. (*C*) Lifetimes in the open (*red*) and closed (*blue*) states as a function of dTTP concentration. Lifetimes were determined from maximum-likelihood fits to the dwell-time distributions similar to those in Fig. 4 *D*. Error bars indicate the 95% confidence intervals. (*D*) Ratio of the lifetimes from (*C*) versus dTTP concentration. All data were recorded at 8 kHz under a constant force of 11.8 pN, using the same hairpin construct as in Fig. 4, MyOne beads, laser illumination, and an intensity of 150 gray levels on the camera. For each dTTP concentration, the hopping transitions were recorded for at least 100 s. To see this figure in color, go online.

CONCLUSIONS

In this work, we have introduced an MT instrument that achieves high spatiotemporal resolution using a fast

GPU-based real-time tracking algorithm (26) together with a laser illumination source (32) to enable camera-based tracking at high (>1 kHz) frame rates. The spatiotemporal resolution of our MT agrees well with the similar work recently described by Seidel and co-workers (29). Our work provides, to our knowledge, the first use of a coherent illumination source in MT, which provides conditions in which the number of photons incident on the sample is no longer a limiting factor for high-speed video tracking. We demonstrate the performance of our apparatus by tracking a single bead in real time at an acquisition rate of 8 kHz over hundreds of seconds, limited only by the speed of the processor (which governs the acquisition rate) and the computer memory (which governs the achievable number of recorded frames). By examining the spatiotemporal resolution of our MT for different bead sizes, illumination sources, illumination intensities, acquisition frequencies, and DNA tethers, we have systematically characterized the conditions that yield the best possible spatiotemporal resolution. We find the best achievable AD to be 0.014 nm for an integration time of 4 s for a surface-attached bead and 0.17 nm for an integration time of 1 s for a tethered dsDNA. We also resolve steps of 0.5 nm with a dsDNA tether and 0.3 nm for a fixed bead. We evaluated different conditions in tether length, tether stiffness, and bead size. We conclude that a short and stiff tether together with small magnetic bead provides the best conditions for the highest spatiotemporal resolution, as predicted by a simple model of Brownian motion in the MT. We also demonstrate that the coherent laser illumination source is compatible with high-spatiotemporal-resolution measurements, substantially reducing the tracking noise. This provides a solution to the problem of the illumination intensity for approximately kilohertz measurements. To illustrate the power of this approach and highlight its, to our knowledge, new capabilities, we have examined the effect of dTTP on the hopping of a DNA hairpin and demonstrated that increased dTTP concentrations bias the hairpin hopping transition toward the unfolded state.

We expect that the high-resolution MT instrument introduced here will provide an attractive approach to detect DNA binding proteins, in particular those that bind only weakly, through the use of a hopping DNA hairpin as an accurate sensor. More generally, high-resolution MT will enable a range of diverse experiments on fast enzyme motion. Together with the ability of MT to observe many tethers in parallel (26,29,31,67) and to integrate fluorescence detection (68,69), MT are an attractive platform to elucidate the mechanics of nucleic acids and other biological polymers and to unravel the mechanochemistry of a diverse set of proteins.

SUPPORTING MATERIAL

Supporting Materials and Methods and five figures are available at http://www.biophysj.org/biophysj/supplemental/S0006-3495(15)01057-7.

AUTHOR CONTRIBUTIONS

D.D. conceived and designed the experiments and built the apparatus. J.C. wrote the tracking software. M.W.D. provided initial help with the software interface. D.D. and T.C. performed the experiments. D.D., T.C., and J.L. analyzed the data. D.D., J.L., and N.H.D. wrote the article.

ACKNOWLEDGMENTS

We thank Francesco Pedaci and Matthew Wiggin for initial help with the software interface, Theo van Laar for providing the DNA hairpin construct, and Zhongbo Yu for help with data acquisition.

Funding is acknowledged from the European Research Council through the DynGenome project and by a TOP grant from the Netherlands Organisation for Scientific Research (NWO), both to N.H.D.

REFERENCES

1. Alberts, B. 2002. Molecular Biology of the Cell. Garland Science, New York.
2. Xie, S. N. 2001. Single-molecule approach to enzymology. *Single Mol.* 2:229–236.
3. Dulin, D., J. Lipfert, …, N. H. Dekker. 2013. Studying genomic processes at the single-molecule level: introducing the tools and applications. *Nat. Rev. Genet.* 14:9–22.
4. Moffitt, J. R., Y. R. Chemla, …, C. Bustamante. 2008. Recent advances in optical tweezers. *Annu. Rev. Biochem.* 77:205–228.
5. Joo, C., H. Balci, …, T. Ha. 2008. Advances in single-molecule fluorescence methods for molecular biology. *Annu. Rev. Biochem.* 77:51–76.
6. De Vlaminck, I., and C. Dekker. 2012. Recent advances in magnetic tweezers. *Annu. Rev. Biophys.* 41:453–472.
7. Neuman, K. C., and S. M. Block. 2004. Optical trapping. *Rev. Sci. Instrum.* 75:2787–2809.
8. Robinson, A., and A. M. van Oijen. 2013. Bacterial replication, transcription and translation: mechanistic insights from single-molecule biochemical studies. *Nat. Rev. Microbiol.* 11:303–315.
9. Li, G. W., and X. S. Xie. 2011. Central dogma at the single-molecule level in living cells. *Nature.* 475:308–315.
10. English, B. P., W. Min, …, X. S. Xie. 2006. Ever-fluctuating single enzyme molecules: Michaelis-Menten equation revisited. *Nat. Chem. Biol.* 2:87–94.
11. Zhuang, X., L. E. Bartley, …, S. Chu. 2000. A single-molecule study of RNA catalysis and folding. *Science.* 288:2048–2051.
12. Lipfert, J., M. M. van Oene, …, N. H. Dekker. 2015. Torque spectroscopy for the study of rotary motion in biological systems. *Chem. Rev.* 115:1449–1474.
13. van Oijen, A. M., and J. J. Loparo. 2010. Single-molecule studies of the replisome. *Annu. Rev. Biophys.* 39:429–448.
14. Kapanidis, A. N., E. Margeat, …, R. H. Ebright. 2006. Initial transcription by RNA polymerase proceeds through a DNA-scrunching mechanism. *Science.* 314:1144–1147.
15. Revyakin, A., C. Liu, …, T. R. Strick. 2006. Abortive initiation and productive initiation by RNA polymerase involve DNA scrunching. *Science.* 314:1139–1143.
16. Larson, M. H., R. Landick, and S. M. Block. 2011. Single-molecule studies of RNA polymerase: one singular sensation, every little step it takes. *Mol. Cell.* 41:249–262.
17. Bustamante, C., W. Cheng, and Y. X. Mejia. 2011. Revisiting the central dogma one molecule at a time. *Cell.* 144:480–497, Erratum in *Cell.* 2011. 145:160.

18. Aitken, C. E., A. Petrov, and J. D. Puglisi. 2010. Single ribosome dynamics and the mechanism of translation. *Annu. Rev. Biophys.* 39:491–513.

19. Holden, S. J., S. Uphoff, …, A. N. Kapanidis. 2010. Defining the limits of single-molecule FRET resolution in TIRF microscopy. *Biophys. J.* 99:3102–3111.

20. Abbondanzieri, E. A., W. J. Greenleaf, …, S. M. Block. 2005. Direct observation of base-pair stepping by RNA polymerase. *Nature.* 438: 460–465.

21. Greenleaf, W. J., M. T. Woodside, …, S. M. Block. 2005. Passive all-optical force clamp for high-resolution laser trapping. *Phys. Rev. Lett.* 95:208102.

22. Cheng, W., S. G. Arunajadai, …, C. Bustamante. 2011. Single-base pair unwinding and asynchronous RNA release by the hepatitis C virus NS3 helicase. *Science.* 333:1746–1749.

23. Strick, T. R., V. Croquette, and D. Bensimon. 2000. Single-molecule analysis of DNA uncoiling by a type II topoisomerase. *Nature.* 404:901–904.

24. Koster, D. A., V. Croquette, …, N. H. Dekker. 2005. Friction and torque govern the relaxation of DNA supercoils by eukaryotic topoisomerase IB. *Nature.* 434:671–674.

25. Chemla, Y. R., K. Aathavan, …, C. Bustamante. 2005. Mechanism of force generation of a viral DNA packaging motor. *Cell.* 122: 683–692.

26. Cnossen, J. P., D. Dulin, and N. H. Dekker. 2014. An optimized software framework for real-time, high-throughput tracking of spherical beads. *Rev. Sci. Instrum.* 85:103712.

27. van Loenhout, M. T., J. W. Kerssemakers, …, C. Dekker. 2012. Non-bias-limited tracking of spherical particles, enabling nanometer resolution at low magnification. *Biophys. J.* 102:2362–2371.

28. Lansdorp, B. M., S. J. Tabrizi, …, O. A. Saleh. 2013. A high-speed magnetic tweezer beyond 10,000 frames per second. *Rev. Sci. Instrum.* 84:044301.

29. Huhle, A., D. Klaue, …, R. Seidel. 2015. Camera-based three-dimensional real-time particle tracking at kHz rates and Ångström accuracy. *Nat. Commun.* 6:5885.

30. De Vlaminck, I., T. Henighan, …, C. Dekker. 2012. Magnetic forces and DNA mechanics in multiplexed magnetic tweezers. *PLoS One.* 7:e41432.

31. Ribeck, N., and O. A. Saleh. 2008. Multiplexed single-molecule measurements with magnetic tweezers. *Rev. Sci. Instrum.* 79:094301.

32. Dulin, D., S. Barland, …, F. Pedaci. 2014. Efficient illumination for microsecond tracking microscopy. *PLoS One.* 9:e107335.

33. Lipfert, J., X. Hao, and N. H. Dekker. 2009. Quantitative modeling and optimization of magnetic tweezers. *Biophys. J.* 96:5040–5049.

34. Lipfert, J., G. M. Skinner, …, N. H. Dekker. 2014. Double-stranded RNA under force and torque: similarities to and striking differences from double-stranded DNA. *Proc. Natl. Acad. Sci. USA.* 111:15408–15413.

35. Vilfan, I. D., J. Lipfert, …, N. H. Dekker. 2009. Magnetic tweezers for single-molecule experiments. *In* Handbook of Single-Molecule Biophysics. P. Hinterdorfer and A. van Oijen, editors. Springer, New York, pp. 371–395.

36. te Velthuis, A. J., J. W. J. Kerssemakers, …, N. H. Dekker. 2010. Quantitative guidelines for force calibration through spectral analysis of magnetic tweezers data. *Biophys. J.* 99:1292–1302.

37. Gosse, C., and V. Croquette. 2002. Magnetic tweezers: micromanipulation and force measurement at the molecular level. *Biophys. J.* 82:3314–3329.

38. Bustamante, C., J. F. Marko, …, S. Smith. 1994. Entropic elasticity of λ-phage DNA. *Science.* 265:1599–1600.

39. Strick, T., J. Allemand, …, D. Bensimon. 2000. Twisting and stretching single DNA molecules. *Prog. Biophys. Mol. Biol.* 74:115–140.

40. Burnham, D. R., I. De Vlaminck, …, C. Dekker. 2014. Skewed brownian fluctuations in single-molecule magnetic tweezers. *PLoS One.* 9:e108271.

41. Wong, W. P., and K. Halvorsen. 2006. The effect of integration time on fluctuation measurements: calibrating an optical trap in the presence of motion blur. *Opt. Express.* 14:12517–12531.

42. Galburt, E. A., S. W. Grill, and C. Bustamante. 2009. Single molecule transcription elongation. *Methods.* 48:323–332.

43. Schäffer, E., S. F. Nørrelykke, and J. Howard. 2007. Surface forces and drag coefficients of microspheres near a plane surface measured with optical tweezers. *Langmuir.* 23:3654–3665.

44. Lansdorp, B. M., and O. A. Saleh. 2012. Power spectrum and Allan variance methods for calibrating single-molecule video-tracking instruments. *Rev. Sci. Instrum.* 83:025115.

45. Czerwinski, F., A. C. Richardson, and L. B. Oddershede. 2009. Quantifying noise in optical tweezers by allan variance. *Opt. Express.* 17:13255–13269.

46. Woodside, M. T., C. García-García, and S. M. Block. 2008. Folding and unfolding single RNA molecules under tension. *Curr. Opin. Chem. Biol.* 12:640–646.

47. Ding, F., M. Manosas, …, V. Croquette. 2012. Single-molecule mechanical identification and sequencing. *Nat. Methods.* 9:367–372.

48. Cheng, W., S. Dumont, …, C. Bustamante. 2007. NS3 helicase actively separates RNA strands and senses sequence barriers ahead of the opening fork. *Proc. Natl. Acad. Sci. USA.* 104:13954–13959.

49. Lionnet, T., A. Dawid, …, V. Croquette. 2006. DNA mechanics as a tool to probe helicase and translocase activity. *Nucleic Acids Res.* 34:4232–4244.

50. Manosas, M., A. Meglio, …, V. Croquette. 2010. Magnetic tweezers for the study of DNA tracking motors. *Methods Enzymol.* 475: 297–320.

51. Ribeck, N., D. L. Kaplan, …, O. A. Saleh. 2010. DnaB helicase activity is modulated by DNA geometry and force. *Biophys. J.* 99:2170–2179.

52. Hänggi, P., P. Talkner, and M. Borkovec. 1990. Reaction-rate theory: fifty years after Kramers. *Rev. Mod. Phys.* 62:251–341.

53. Bustamante, C., Y. R. Chemla, …, D. Izhaky. 2004. Mechanical processes in biochemistry. *Annu. Rev. Biochem.* 73:705–748.

54. Woodside, M. T., W. M. Behnke-Parks, …, S. M. Block. 2006. Nanomechanical measurements of the sequence-dependent folding landscapes of single nucleic acid hairpins. *Proc. Natl. Acad. Sci. USA.* 103:6190–6195.

55. Dessinges, M. N., B. Maier, …, V. Croquette. 2002. Stretching single stranded DNA, a model polyelectrolyte. *Phys. Rev. Lett.* 89:248102.

56. Woodside, M. T., P. C. Anthony, …, S. M. Block. 2006. Direct measurement of the full, sequence-dependent folding landscape of a nucleic acid. *Science.* 314:1001–1004.

57. Bell, G. I. 1978. Models for the specific adhesion of cells to cells. *Science.* 200:618–627.

58. Liphardt, J., B. Onoa, …, C. Bustamante. 2001. Reversible unfolding of single RNA molecules by mechanical force. *Science.* 292:733–737.

59. Anthony, P. C., A. Y. Sim, …, D. Herschlag. 2012. Electrostatics of nucleic acid folding under conformational constraint. *J. Am. Chem. Soc.* 134:4607–4614.

60. Dittmore, A., J. Landy, …, O. A. Saleh. 2014. Single-molecule methods for ligand counting: linking ion uptake to DNA hairpin folding. *J. Am. Chem. Soc.* 136:5974–5980.

61. Johnson, D. S., L. Bai, …, M. D. Wang. 2007. Single-molecule studies reveal dynamics of DNA unwinding by the ring-shaped T7 helicase. *Cell.* 129:1299–1309.

62. Manosas, M., M. M. Spiering, …, S. J. Benkovic. 2012. Collaborative coupling between polymerase and helicase for leading-strand synthesis. *Nucleic Acids Res.* 40:6187–6198.

63. Wen, J. D., L. Lancaster, …, I. Tinoco. 2008. Following translation by single ribosomes one codon at a time. *Nature.* 452:598–603.

64. Ibarra, B., Y. R. Chemla, …, C. Bustamante. 2009. Proofreading dynamics of a processive DNA polymerase. *EMBO J.* 28:2794–2802.

65. Morin, J. A., F. J. Cao, …, B. Ibarra. 2012. Active DNA unwinding dynamics during processive DNA replication. *Proc. Natl. Acad. Sci. USA.* 109:8115–8120.

66. Manosas, M., M. M. Spiering, …, V. Croquette. 2012. Mechanism of strand displacement synthesis by DNA replicative polymerases. *Nucleic Acids Res.* 40:6174–6186.

67. De Vlaminck, I., T. Henighan, …, C. Dekker. 2011. Highly parallel magnetic tweezers by targeted DNA tethering. *Nano Lett.* 11:5489–5493.

68. van Loenhout, M. T., M. V. de Grunt, and C. Dekker. 2012. Dynamics of DNA supercoils. *Science.* 338:94–97.

69. Schwarz, F. W., J. Tóth, …, R. Seidel. 2013. The helicase-like domains of type III restriction enzymes trigger long-range diffusion along DNA. *Science.* 340:353–356.

Supporting Materials for:

High Spatiotemporal-Resolution Magnetic Tweezers: Calibration and Applications for DNA Dynamics

David Dulin,[1,*], Tao Ju Cui,[1] Jelmer Cnossen,[1] Margreet W. Docter,[1] Jan Lipfert,[2] and Nynke H. Dekker[1,*]

[1]Department of Bionanoscience, Kavli Institute of Nanoscience, Delft University of Technology, Delft, The Netherlands; and [2]Department of Physics, Nanosystems Initiative Munich and Center for Nanoscience, Ludwig-Maximilians-University Munich, Munich, Germany

*To whom the correspondence maybe addressed: daviddulin82@gmail.com or n.h.dekker@tudelft.nl

This document contains Supplementary Text and 5 Supplementary Figures.

Supplementary Text

Spatiotemporal resolution for surface-melted beads as a function of illumination intensity and bead size

As discussed in the main text, the light intensity available for sample illumination is a factor that must be carefully considered in high-speed video tracking. At low light intensities, the tracking noise will become the limiting factor; conversely, at saturating illumination intensities, the lack of contrast between the rings in the diffraction pattern will become limiting. Here, we characterize the achievable spatiotemporal resolution as a function of the illumination light intensity (**Fig. S3**) prior to testing the optimal configuration (**Fig. 2B**).

To quantify the light intensity in the field of view, we average the discrete grey levels of the camera (8 bits, corresponding to 256 grey levels) over the entire field of view. We observe a significant increase in resolution for light illumination intensities that yield a camera response up to 200 grey levels (**Fig. S3A-F**). However, the improvement in the resolution of bead positions levels off for light intensities exceeding 150 grey levels; we achieve an optimal resolution of 0.014 nm at 4 s using 175 grey levels for a trace acquired at 500 Hz under LED illumination (**Fig. S3C,F**). This same trend is observed for beads of different types: MyOne magnetic beads (1 μm diameter, **Fig. S3A**), small latex beads (1.5 μm diameter, **Fig. S3B**), M270 beads

(2.8 μm diameter, **Fig. S3C**), and large latex beads (3 μm diameter, **Fig. S3D**): spatial resolution always improves with increased illumination intensity (until 200 grey levels, **Fig. S3E**) and with longer averaging times τ, until drift becomes limiting at τ ~1-10 s.

We also evaluate how the achievable spatial resolution differs for these types of surface-melted beads (**Fig. S3**). First, we observe that a bead's material composition (magnetic vs. latex) does not impact the achievable resolution (**Fig. S3F**, compare polystyrene beads in red and magnetic beads in blue). However, we do see a two-fold improvement in spatial resolution when we use larger beads (dashed lines for smaller beads, plain lines for larger beads, **Fig. S3F**). For example, in the case of M270 beads (solid blue line, **Fig. S3F**), the Allan deviation (AD) equals 0.1 nm and 0.02 nm over time intervals of 0.01 s and 1 s, respectively, while in the case of MyOne beads, the AD is limited to 0.4 nm and 0.04 nm over the same time intervals (dashed blue line, **Fig. S3F**). This result is in agreement with the recent work of Seidel and co-workers (29) in which they observed an improvement of the spatiotemporal resolution using larger beads and a reduction in AD with the averaging temporal window, following a power law in $1/\sqrt{N}$, identically to our results. We represent the Allan deviation for a given time interval (0.13 s) from **Fig. S3F** as a function of the bead size (blue circle, **Fig. S3G**) and we observed that the AD decreases as $1/R_{bead}$ (black solid line, **Fig. S3G**). This observation is consistent with a scattered light intensity described by the Mie theory ($I_{scatt} \propto 1/R_{bead}^2$), which is valid for a sphere with a radius larger than the wavelength of the illumination light, and an AD following a power law of the form $1/\sqrt{I}$ (solid red line, **Fig. S3E**). If the scattered light intensity was described by the Rayleigh theory (valid for sub-wavelength radius objects), the AD would have decayed as $1/R_{bead}^3$ (black dashed line, Fig. S3G), which does not fit our experimental results.

Spatiotemporal resolution of a dsDNA or a ssDNA tethered beads determined from numerical simulation.

We simulate the fluctuations z-axis of a magnetic bead of 1 μm diameter tethered to a 1.9 kbp DNA, and experiencing a force of 18 pN (**Fig. S4**) (43). We simulated traces

for duration of 3 s, sampled at 0.1 μs, subsequently boxcar-filtered at either 8 kHz or 500 Hz to simulate the camera shutter time used in our experiments. We first perform simulations in the absence of tracking noise: in this case, theory predicts (Eq. 3) that traces acquired at different acquisition frequencies should display identical values of the AD for a given time window. This prediction is confirmed by our numerical simulations: the AD of box-car filtered traces acquired at 8 kHz (dashed pink line, **Fig. S4A**) and 500 Hz (solid pink line, **Fig. S4A**) are identical. Next, we add Gaussian noise with a standard deviation of 1 nm to these simulated traces to mimic the tracking noise on a 1 μm diameter magnetic bead (**Fig. S3A-F**). A comparison of two simulated traces at 8 kHz in the absence (dashed pink line, **Fig. S4B**) and presence of noise (dashed purple line, **Fig. S4B**) shows how the AD increases in the presence of tracking noise, as it should since the total noise is the quadratic sum of the thermal noise and the tracking noise. Lastly, we compare simulated traces with tracking noise at the two different acquisition frequencies, 8 kHz (dashed purple line, **Fig. S4C**) and 500 Hz (solid purple line, **Fig. S4C**). The trace simulated at 8 kHz displays a clear improvement in the magnitude of the AD, as the tracking noise is averaged as $1/\sqrt{N}$ (**Fig. S3F**).

Similarly to the dsDNA-tethered bead, we simulate the fluctuations along the z-axis for the case of an open hairpin, e.g. a ssDNA-tethered bead. In short, we simulate a 1 μm diameter magnetic bead tethered to a 2 kb ssDNA under a force of 19 pN (**Fig. S4**). The simulated traces are sampled at 1 μs for a duration of 10 s, and subsequently boxcar-filtered at either 8 kHz or 500 Hz to simulate the camera shutter time employed. As above, the numerical simulations show that the AD of traces box-car filtered at either 8 kHz (dashed green line, **Fig. S4A**) or 500 Hz (solid green line, **Fig. S5B**) are identical for a given time window. Adding Gaussian noise of 1 nm standard deviation to the simulated traces at 8 kHz and 500 Hz, we observe no change in ADs (**Fig. S5B-C**), confirming what we observed experimentally in **Fig. 3D**, meaning that the resolution is limited by the thermal noise. In that case, a faster acquisition rate does not provide a better spatiotemporal resolution.

Spatiotemporal resolution for DNA-hairpin tethered beads as a function of bead size and tether length

In the main text, we discuss the spatiotemporal resolution of dsDNA- and hairpin-tethered beads. For both types of tethers, considerations of the bead radius and the tether length and nature (Eqs. 2,3 of the main text) need to be taken into account. As an example, we here consider the bead-size and tether-length considerations for hairpin-tethered beads (**Fig. 1A**).

Generally speaking, temporal resolution for a tethered bead is expected to improve with smaller beads and shorter tethers, as can be deduced from Eq. 5 of the main text, which indicates that the bandwidth of the system scales with these two parameters. As a consequence, providing a tether-bead system with a larger bandwidth offers the possibility to observe fast enzymatic steps. However, when using a smaller magnetic bead, it is important to not be limited by the loss in tracking accuracy.

To test the effect of the bead size on the spatiotemporal resolution, we compare the thermal noise for beads of different diameters (1 μm diameter MyOne beads, black lines in **Fig. S5E**; 2.8 μm diameter M270 beads; grey lines in **Fig. S5E**) located ~200 nm away from the flow chamber surface (**Fig. 1A**) via hairpin tethering (**Fig. 1A**). As in the main text, the comparison is performed by computing the respective AD along the *z* axis. For M270 beads, we acquire data at 2 kHz with a high-power fiber-coupled LED illumination, whereas for MyOne beads, we acquire data at 4 kHz using laser-based illumination (**Fig. S5A**). For both bead types, we first compare the noise for closed hairpins (force ~12 pN, solid lines in **Fig. S5E**). We observe that the AD peak is shifted to shorter timescales for MyOne beads (black solid lines, **Fig. S5E**) compared to M270 beads (grey solid lines, **Fig. S5B**), with corresponding peak amplitudes of ~2 nm at ~0.25 ms and ~3 nm at ~3 ms, respectively. Given that the hairpin handle is predominantly composed of dsDNA, we initially model these tethers as double-stranded nucleic acids with an extension of 200 nm (and a persistence length L_P of 50 nm). For both bead types, theory predicts peak amplitudes of 1.2 nm that are comparable to experimental observations; however, it also predicts timescales of 0.023 and 0.26 ms, respectively, th at are found to be ten-fold shorter than experimentally observed. To understand this discrepancy in timescales, we revise the modeling, assuming that the handles perform mechanically as if they predominantly consisted of ssDNA (with $L_P = 0.5$ nm). In doing so, we obtain much better agreement with the experimental results (predicted peak amplitudes of 2.7 nm for

both bead types, with timescales of 0.12 ms and 1.3 ms, respectively). This result implies that the single-stranded portions of the handles dominate the dynamics of our bead-closed hairpin system. On longer timescales, we note that the AD continues to decrease until drift starts to dominate at $\tau > 1$ s (**Fig. S5E**) (31, 46) for both bead types. At the local minimum of the AD, we measure amplitudes of ~ 0.3 nm for MyOne beads and ~ 0.6 nm for M270 beads. These values exceed theoretical predictions (under the assumption of predominantly ssDNA handles) by factors of 8 and 4, respectively. This increased noise observed experimentally may result from hairpin dynamics, e.g. slow partial fraying and reannealing of the hairpin, that dominate the noise on longer timescales.

Using a smaller bead provides a smaller correlation time for a similar AD peak amplitude, hence the spatiotemporal resolution is improved for an equivalent time averaging window (Eq. 3 in the main text) larger than the correlation time of the system (**Fig. S5E**).

We have also examined the spatiotemporal response of different bead types that are tethered to open hairpins (force ~19 pN, $k_z \sim 0.55\ pN/nm$, dashed lines in **Fig. S5E**). We measure that the peak of the AD for M270 beads lies at ~1 ms (grey dashed line, **Fig. S5E**), whereas it lies at ~0.25 ms for MyOne beads (black dashed line, **Fig. S5E**; with some uncertainly as it is difficult to accurately determine the peak position here), with an amplitude of ~ 4 nm for both beads. Our model (assuming a ssDNA extension of 1 μm), predicts peak amplitudes of 6 nm located at 0.25 ms for MyOne beads and at 1.8 ms for M270 beads, in good agreement with the experimental results. On longer timescales (~1 s), the experimentally measured peak AD amplitudes of ~ 0.2 nm for MyOne beads and ~ 0.3 nm for M270 beads match up well with theoretical predictions (0.14 nm for MyOne beads; 0.37 nm for M270 beads). Thus, the gain in bandwidth by using smaller beads with open hairpins provides an improved spatiotemporal resolution, as in the case of beads tethered to closed hairpins. These results confirm the prediction that one should employ the smallest possible beads to maximize the information that can be extracted at short timescales (6), as this allows one to attain, upon averaging to a lower bandwidth, increased spatiotemporal resolution. We note in particular that this result is, independent of whether a bead is tethered to a closed or open hairpin. The agreement between theory

and experiment furthermore highlight how the simple model that we introduce can be successfully employed to evaluate the spatiotemporal response for a tethered molecule. This can be useful to experimentalists as it allows one to design experimental conditions in order to observe catalytic activity at optimal resolution.

Lastly, we investigate the effect of tether length on the spatiotemporal resolution achievable with DNA hairpins, where we expect that the use of a short, and therefore stiff construct (**Fig. 1B**), will provide the best spatiotemporal resolution (Eq. (2) in the main text) when using the same type of bead. We compare the AD for closed hairpins with ~200 nm and ~700 nm handles, respectively. For both cases, we employ 1 μm diameter MyOne beads and laser illumination. The AD of the hairpin with the 700 nm handle peaks at ~0.4 ms with a magnitude of ~5 nm (**Fig. S5F**, black arrows), which compares well to the theoretically computed values of 0.2 ms and 5 nm (ssDNA handles, Eqs. 3, 5 of the main text). As expected, the hairpin with the 200 nm handle provides improved spatiotemporal resolution, with an AD that peaks at ~0.25 ms with a magnitude of ~2 nm (**Fig. S5F,** solid blue line). Over a time interval of 1 s, we measure an AD of 0.3 nm at 1 s for the hairpin with the ~200 nm handle (**Fig. S5F**, blue solid line), which is a three-fold improvement over the AD of 0.9 nm for the hairpin with the ~200 nm handle (**Fig. S5F**, blue dashed line). However, on this timescale the experimentally measured values are tenfold higher than theoretical predictions, which yield 0.1 nm (0.04 nm) for the hairpin with the longer (shorter) handle. The origin of the discrepancy is likely common to both two hairpins and may derive from slow hairpin dynamics, as described above. From these results, we conclude that the gain in noise reduction and bandwidth through the use of a shorter (hence stiffer) molecule exceeds any reductions in bandwidth that result from the increased friction associated with surface proximity, as predicted by theory (Eqs. 3, 5, 6 of the main text, **Fig. 1B**).

Oligonucleotides involved in the hairpin design of Figure S1 (polarity: 5'->3')

1-kb fragment:

CTCCTGTGTGGTCTCGTTGCGAAGTAGTTATTAGCCACCCAGGAACCAAAAAAAAAA
AAAAAAAAAAAAAAAAAAAAAAAAAAAAAAAAAAAAAAAAAAAAAAAAAAAAAAAA
AAAAAAAAAAAAAAAAAAAAAAAAAAAAAAAAAAAAAAAAAAAAAAAAAAAAAAAA

AAAAAAAAAAAAAAAAAAAACTCGAGGAGCTTGGCACTGGCCGTCGTTTTACAACGT
CGTGACTGGGAAAACCCTGGCGTTACCCAACTTAATCGCCTTGCAGCACATCCCCCTT
TCGCCAGCTGGCGTAATAGCGAAGAGGCCCGCACCGATCGCCCTTCCCAACAGTTGCG
CAGCCTGAATGGCGAATGGCGCCTGATGCGGTATTTTCTCCTTACGCATCTGTGCGGT
ATTTCACACCGCATATGGTGCACTCTCAGTACAATCTGCTCTGATGCCGCATAGTTAA
GCCAGCCCCGACACCCGCCAACACCCGCTGACGCGCCCTGACGGGCTTGTCTGCTCCC
GGCATCCGCTTACAGACAAGCTGTGACCGTCTCCGGGAGCTGCATGTGTCAGAGGTT
TTCACCGTCATCACCGAAACGCGCGAGACGAAAGGGCCTCGTGATACGCCTATTTTTA
TAGGTTAATGTCATGATAATAATGGTTTCTTAGACGTCAGGTGGCACTTTTCGGGGA
AATGTGCGCGGAACCCCTATTTGTTTATTTTTCTAAATACATTCAAATATGTATCCG
CTCATGAGACAATAACCCTGATAAATGCTTCAATAATATTGAAAAAGGAAGAGTATG
AGTATTCAACATTTCCGTGTCGCCCTTATTCCCTTTTTTGCGGCATTTTGCCTTCCTG
TTTTTGCTCACCCAGAAACGCTGGTGAAAGTAAAAGATGCTGAAGATCAGTTGGGTG
CACGAGTGGGTTACATCGAACTGGATCTCAACAGCGGTAAGATCCTTGAGAGTTTTC
GCCCCGAAGAACGTTTTCCAATGATGAGCACTTTTAAAGTTCTCCTAGGAGACCCGG
TATTATC

Primer 1458:
GGCCAACCAAGTCATTCTGAGAATAGTGTATGCGGCGACCGAGTTGCTCTTGCCTTT
TTTTTTTATGCTCTTTACAACCGGTTGACTGCTTCAGGGGTCGATCCCGCTTTGTAC
Primer 1459:
GCAAGTACAAAGCGGGATCGACCCCTGAAGCAGTCAACCGGTTGTAAAGAGCATGCC
AGATGGTAAGCCCTCCCGTATCGTAGTTATCTACACGACGGGGAGTCAGGCAACTAT
GGATGAACGA
Primer 1460:
GATCTCGTTCATCCATAGTTGCCTGACTCCCCGTCGTGTAGATAACTACGATACGGGA
GGGCTTACCATCTGGC
Primer 1461:
ATTCTCAGAATGACTTGGTT
Primer 1462:
GAGCAACTCGGTCGCCGCATACACTATTCTCAGAATGACTTGGTT
Primer 1531:
CCTAAGCTCGCCGAGGCGAGCGAAAGCTCGCCTCGGCGAGCT

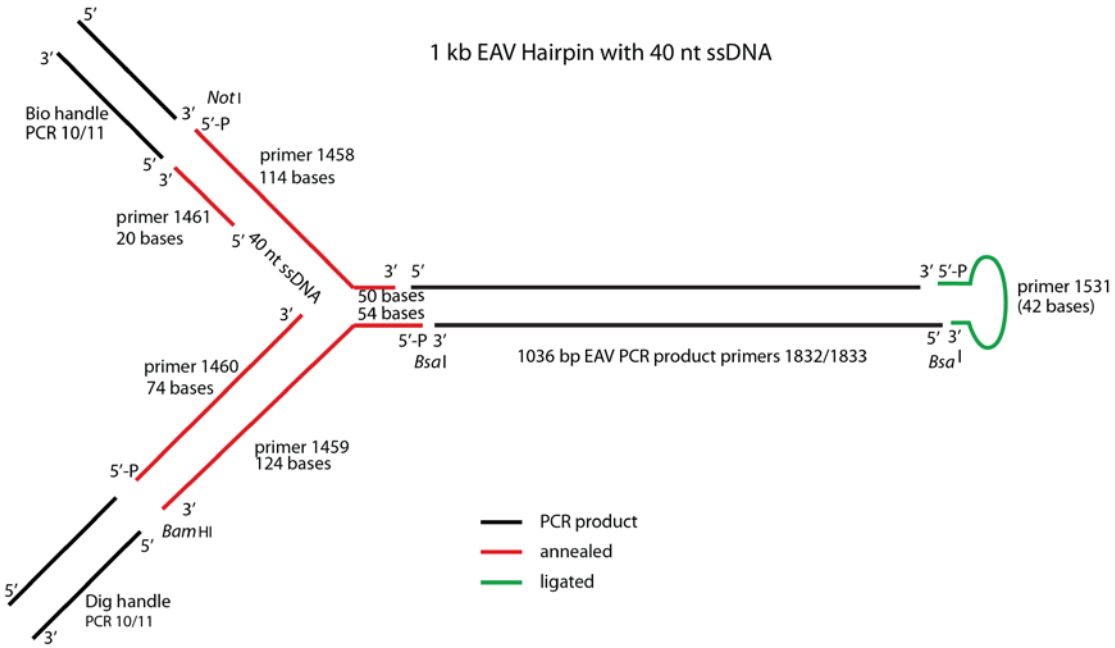

Figure S1: Hairpin design described in the Materials and Methods of the main text and used for the studies detailed in Figures 3, 4, 5.

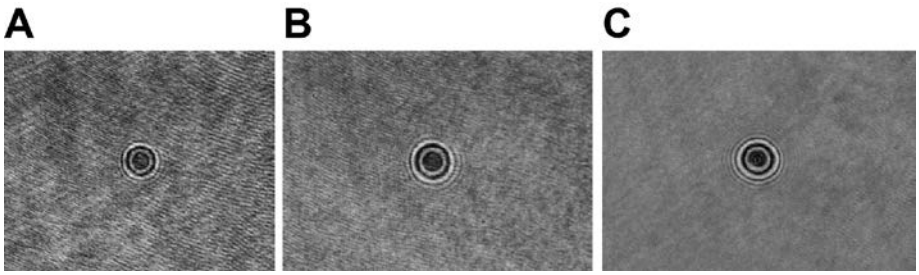

Figure S2: Field of view with a surface-melted M270 magnetic bead in different conditions of laser-based illumination: Without fast modulation and without per-pixel linear correction (**Materials and Methods**) **(A)**, With fast modulation and without per-pixel linear correction **(B)**, With fast modulation and with per-pixel linear correction **(C)**.

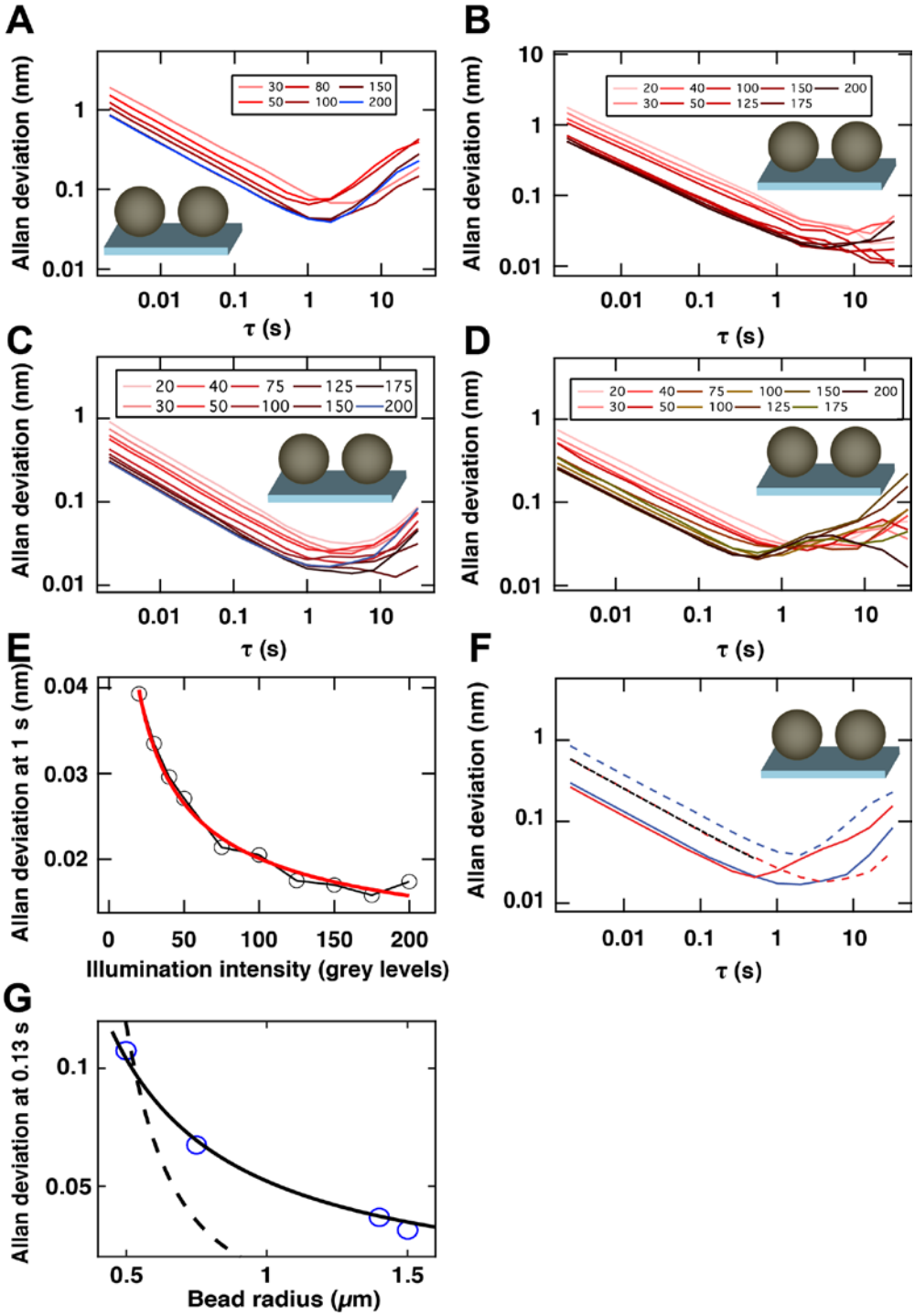

Figure S3: Allan deviation along the z-axis for different types of surface melted beads and illumination intensities. (A) A 1 μm diameter MyOne magnetic bead. **(B)** 1.5 μm diameter polystyrene bead. **(C)** A 2.8 μm diameter M270 beads. **(D)** A 3 μm diameter polystyrene bead. For τ>1 s, we observed an increase in the values of the AD. This increase in the AD values results from a lower statistics at large τ, which depends on the duration of the measurement. **(E)** The Allan deviation measured in (B) at 1 s is represented as a function of the light intensity on the camera (grey levels). The red line is a fit to the Allan deviation at 1s to a power law of the form $A \cdot I^x$, yielding $x = -0.55 \pm 0.13$, I being the average intensity on the camera. **(F)** Comparison of the Allan deviations for different types of surface-melted beads and 200 grey levels:

Myone beads (1 μm diameter, blue dashed line); small latex beads (1.5 μm diameter, red dashed line); M270 beads (2.8 μm diameter, blue solid line); and large latex beads (3 μm diameter, red solid line). Black dashed line: fit to the data for the small latex bead to a power law of the form $A \cdot \tau^x$, yielding $x = -0.52 \pm 0.05$. To acquire these datasets, we employ high-power LED illumination and perform real-time tracking at an acquisition frequency of 500 Hz. In all cases, the position of the tracked bead is corrected for drift via reference bead subtraction (**Fig. 1A**). **(G)** The Allan deviation measured at 0.13 s in (F) is represented as a function of the bead radius (blue circle). The black solid line and the black dashed line are fits of the form $1/R_{bead}$ and $1/R_{bead}^3$, respectively.

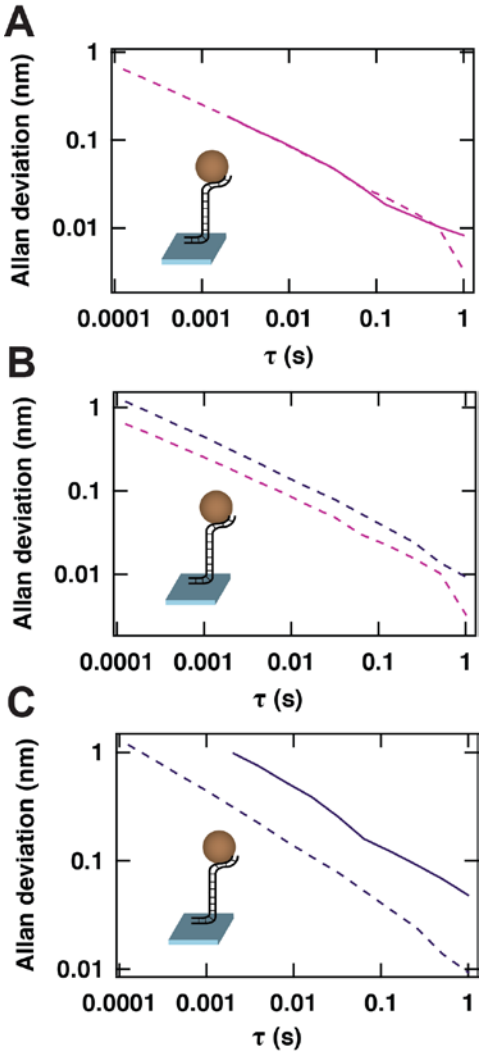

Figure S4: Numerical simulations to determine the resolution along the z-axis for a tethered magnetic bead when the noise is dominated by the tracking noise. From a numerical simulation of the motion of a 1 µm diameter magnetic bead tethered to a 1.9 kbp long dsDNA experiencing a force of 18 pN (simulation total duration: 5 s; sampling time: 0.1 µs), we compare: **(A)** the Allan deviation of the z-position for a boxcar-filtered 8 kHz trace (dashed pink line) and a boxcar-filtered 500 Hz (solid pink line); **(B)** the Allan deviation of the z-position for a boxcar-filtered 8 kHz trace (dashed pink line) and the same trace including an additional gaussian noise of 1 nm standard deviation to simulate the tracking noise (dashed purple line); **(C)** the Allan deviation of the z-position for a boxcar-filtered 8 kHz trace (dashed purple line) and a boxcar-filtered 500 Hz (solid purple line), both including an additional a gaussian noise of 1 nm standard deviation to simulate the tracking noise.

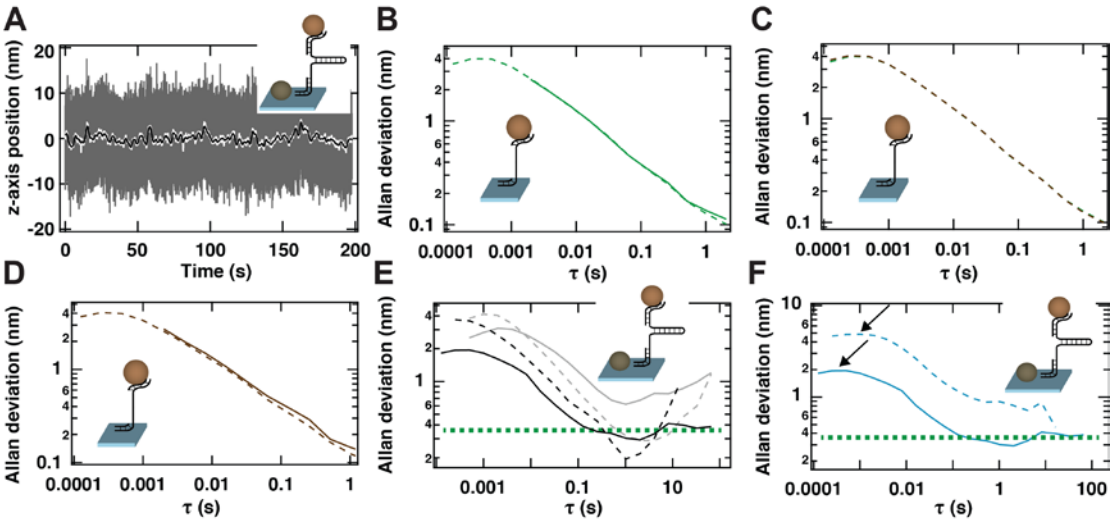

Figure S5: Experiments and numerical simulations to determine the resolution along the z-axis for a tethered magnetic bead when the noise is dominated by the thermal noise. (A) Typical trace of the tracked position along the *z*-coordinate of MyOne magnetic bead tether on a DNA hairpin with an applied force of ~12 pN. We use a laser-based illumination, the number of grey levels is set to 150, and real-time tracking is performed at 4 kHz simultaneously for the tethered bead and a surface-melted reference bead, whose position along the *z*-axis has been subtracted. Grey line: raw data, white line: box-car filtered 10 Hz, black line: box-car filtered 1Hz. From a numerical simulation of the motion of a 1 μm diameter magnetic bead tethered to a 2 kb long ssDNA experiencing a force of 19 pN (simulation total duration: 3 s; sampling time: 0.1 μs), we compare: **(B)** the Allan deviation of the z-position for a boxcar-filtered 8 kHz trace (dashed green line) and a boxcar-filtered 500 Hz (solid green line); **(C)** the Allan deviation of the z-position for a boxcar-filtered 8 kHz trace (dashed green line) and the same trace including an additional gaussian noise of 1 nm standard deviation to simulate the tracking noise (dashed brown line); **(D)** the Allan deviation of the z-position for a boxcar-filtered 8 kHz trace (dashed brown line) and a boxcar-filtered 500 Hz (solid brown line), both including an additional gaussian noise of 1 nm standard deviation to simulate the tracking noise. **(E)** The Allan deviation of the *z*-position for DNA hairpin-tethered MyOne (black dashed and solid lines) and M270 (grey dashed and solid lines) beads. The reference bead position has been subtracted from that of the hairpin-tethered beads prior to computation of the Allan deviation. Illumination is provided by a high power fiber-coupled LED for the M270 beads and using laser illumination for the MyOne beads, the number of grey levels is set to 150, real-time tracking is performed at 2 kHz for M270 beads and at 4 kHz for MyOne beads, and the applied force equals either ~19 pN (open hairpin, dashed lines) or ~12 pN (closed hairpin, solid lines) **(F)** The Allan deviation of the *z*-position of dsDNA hairpin-tethered MyOne beads, where the length of the tether handles is either ~200 nm (blue solid line) or ~700 nm (blue dashed line), with both beads position corrected by subtracting a reference bead position. Illumination is provided by a laser, the number of grey levels is set to 150, real-time tracking is performed at 8 kHz for the tethers with short handles and at 4 kHz for the tethers with long handles, and the applied force equals ~12 pN (closed hairpin).

The arrows indicate the positions of the peak position of the AD of the bead-DNA hairpin system.